Biomaterials 302 (2023) 122300

Contents lists available at ScienceDirect

Biomaterials

journal homepage: www.elsevier.com/locate/biomaterials

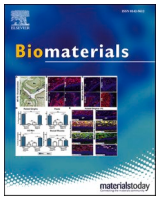

A STING pathway-activatable contrast agent for MRI-guided tumor immunoferroptosis synergistic therapy

Shuai Guo [a], Wei Xiong [b], Jiaoyang Zhu [a], Jie Feng [b], Ruilong Zhou [a], Qingdeng Fan [a], Qianqian Zhang [a], Zongheng Li [a], Jing Yang [a], Huimin Zhou [c], Peiwei Yi [a], Yanqiu Feng [a], Sugeun Yang [d], Xiaozhong Qiu [c], Yikai Xu [b], Zheyu Shen [a,*]

[a] School of Biomedical Engineering, Southern Medical University, 1023 Shatai South Road, Guangzhou, Guangdong, 510515, China
[b] Medical Imaging Center, Nanfang Hospital, Southern Medical University, 1023 Shatai South Road, Guangzhou, Guangdong, 510515, China
[c] Guangdong Provincial Key Laboratory of Construction and Detection in Tissue Engineering, School of Basic Medical Sciences, Southern Medical University, 1023 Shatai South Road, Guangzhou, Guangdong, 510515, China
[d] Department of Biomedical Science, BK21 FOUR Program in Biomedical Science and Engineering, Inha University College of Medicine, Incheon, 22212, South Korea

ARTICLE INFO

Keywords:
Magnetic resonance imaging (MRI)
Contrast agents (CAs)
Stimulator of interferon genes (STING)
Enhanced ferroptosis therapy
Immunoferroptosis synergistic therapy

ABSTRACT

The immunotherapy efficiency of stimulator of interferon genes (STING)-activatable drugs (*e.g.*, 7-ethyl-10-hydroxycamptothecin, SN38) is limited by their non-specificity to tumor cells and the slow excretion of the DNA-containing exosomes from the treated cancer cells. The efficacy of tumor ferroptosis therapy is always limited by the elimination of lipid peroxides (LPO) by the pathways of glutathione peroxidase 4 (GPX4), dihydroorotate dehydrogenase (DHODH) and ferroptosis suppressor protein 1(FSP1). To solve these problems, in this study, we developed a STING pathway-activatable contrast agent (*i.e.*, FeGd-HN@TA-Fe^{2+}-SN38 nanoparticles) for magnetic resonance imaging (MRI)-guided tumor immunoferroptosis synergistic therapy. The remarkable *in vivo* MRI performance of FeGd-HN@TA-Fe^{2+}-SN38 is attributed to its high accumulation at tumor location, the high relaxivities of FeGd-HN core, and the pH-sensitive TA-Fe^{2+}-SN38 layer. The effectiveness and biosafety of the immunoferroptosis synergistic therapy induced by FeGd-HN@TA-Fe^{2+}-SN38 are demonstrated by the *in vivo* investigations on the 4T1 tumor-bearing mice. The mechanisms of *in vivo* immunoferroptosis synergistic therapy by FeGd-HN@TA-Fe^{2+}-SN38 are demonstrated by measurements of *in vivo* ROS, LPO, GPX4 and SLC7A11 levels, the intratumor matured DCs and $CD8^+$ T cells, the protein expresion of STING and IRF-3, and the secretion of IFN-β and IFN-γ.

1. Introduction

Ferroptosis therapy (FT) of tumors aims to initiate the programmed cells death by accumulated lipid peroxides (LPO), which is generated from the oxidative stress in cells [1–4]. Despite the significant breakthrough in ferroptosis acceleration by ascending the level of intracellular reactive oxygen species (ROS), the overall efficiency of LPO generation and accumulation still remains unsatisfactory due to the natural ferroptosis defense in cells [5]. According to the recent insights into the ferroptosis regulation mechanisms, there are three parallel pathways that respond to the prevention of ferroptosis, including glutathione (GSH) peroxidase 4 (GPX4) pathway [2,6], ferroptosis suppressor protein 1 (FSP1) pathway [7] and dihydroorotate dehydrogenase (DHODH)-mediated ferroptosis defense pathway [8]. Typically, the GPX4 converts the cytotoxic LPO into the nontoxic lipid alcohol with consumption of GSH as the substrate. The FSP1 catalyzes the recycling of coenzyme Q10 (CoQ10) to ubiquinol ($CoQ10H_2$) by consumption of lipid peroxyl radicals, which prevents LPO accumulation. The DHODH attenuates ferroptosis by inhibition of mitochondrial LPO with reducing ubiquinone to ubiquionol. Consequently, the further development of new strategies to inhibit the above-mentioned three ferroptosis defense pathways is very significant to enhance the LPO accumulation for ferroptosis therapy of tumors [2,7–21].

The cancer immunotherapy-activated $CD8^+$ T cells mainly clear tumor cells *via* the Fas-Fas ligand pathway [22]. Meanwhile, the released interferon (IFN)-γ from $CD8^+$ T cells can downregulate the expression of SLC3A2 and SLC7A11 that are the subunits of the glutamate-cystine antiporter system (X_c^-), which thus inhibit the cellular

* Corresponding author.
E-mail address: sz@smu.edu.cn (Z. Shen).

https://doi.org/10.1016/j.biomaterials.2023.122300
Received 24 March 2023; Received in revised form 9 August 2023; Accepted 28 August 2023
Available online 29 August 2023

uptake of L-cystine, further suppress the bioactivity of GPX4, enhance the LPO accumulation in cancer cells, and then promote the ferroptosis of tumor cells [22]. Recently, nanomedicines with the function of stimulator of interferon genes (STING) activation have been widely used for cancer immunotherapy applications *via* an endogenously activated cyclic guanosine monophosphate (GMP)-adenosine monophosphate (AMP) synthase (cGAS)-STING pathway. Typically, the cGAS recognizes and binds to cytosolic tumor DNA, forming cyclic GMP-AMP (cGAMP) that is the natural ligand of STING. The binding of cGAMP and STING can further recruit TANK-binding kinase 1 (TBK1), activate interferon regulatory factor (IRF)-3 and induce IFN-β generation, which can further promote the dendric cells (DCs) migration, activate the cytotoxic T lymphocytes cells (*i.e.* $CD8^+$ T cells) and natural killer (NK) cells, and enhance the IFN-γ secretion [13,23–41]. Zhao J. et al. screened a potent drug 7-ethyl-10-hydroxycamptothecin (SN38) for STING activation, which was proved to be mediated by the DNA-containing exosomes from the SN38 treated cancer cells. After transferring to bone marrow dendric cells (BMDCs), the DNA-containing exosomes can activate the STING pathway, and stimulate IFN-β secretion followed by robust activation of NK cells and $CD8^+$ T cells [35,36,38,40–45]. However, the immunotherapy efficiency of STING-activatable drugs (*e.g.*, SN38) is limited by their non-specificity to tumor cells and the slow excretion of the DNA-containing exosomes from the treated cancer cells.

Illuminated by the previous work that developing integrated model for tumor diagnosis and therapy [46,47], in this study, the above-mentioned problems of ferroptosis therapy and immunotherapy were solved by developing a STING pathway-activatable contrast agent (CA) for MRI-guided tumor immunoferroptosis synergistic therapy (Scheme 1). Typically, Fe_3O_4/Gd_2O_3 hybrid nanoparticles (FeGd-HN), a superior T_1-weighted MRI contrast agent (CA) with high longitudinal relaxivity r_1 (70.0 mM^{-1} s^{-1}), low r_2/r_1 ratio (1.98, r_2 is transverse relaxivity), small particle size (~5.5 nm), good water dispersibility and stability [48], is utilized for coating of tannic acid (TA) and complexing of Fe^{2+} and SN38, generating FeGd-HN@TA-Fe^{2+}-SN38. After intravenous injection, FeGd-HN@TA-Fe^{2+}-SN38 accumulates at solid tumors due to the enhanced permeability and retention (EPR) effect. Under the acidic tumor environment (TME) and endosome conditions, TA, Fe^{2+} and SN38 can be released from FeGd-HN@TA-Fe^{2+}-SN38. The generated FeGd-HN can be used for high contrast MRI of tumors. The released Fe^{2+} can initiate ferroptosis *via* Fenton reaction with intracellular H_2O_2 ($Fe^{2+} + H_2O_2 \rightarrow Fe^{3+} + \bullet OH + OH^-$), generating •OH and Fe^{3+}. The released TA plays a role of transferring Fe^{3+} to Fe^{2+} due to the electron transferring from the ortho-phenolic hydroxyl groups of TA to Fe^{3+}, which benefits the ferroptosis *via* Fenton reaction. The produced robust ROS results in GSH/GPX4 downregulation, LPO accumulation, cell membrane rupture, and cell ferroptosis. The released SN38 can activate the STING pathway *via* the DNA-containing exosomes, stimulate IFN-β secretion, and activate NK and $CD8^+$ T cells for immunotherapy. The cell membrane rupture facilitates the release of DNA-containing exosomes for further activation of STING pathway. Robust IFN-γ secretes in the activated STING pathway, which can inhibit the system X_c^- and activate the GPX4 pathway, leading to LPO accumulation for ferroptosis therapy. Therefore, our MRI contrast agent FeGd-HN@TA-Fe^{2+}-SN38 can be used for immunoferroptosis synergistic therapy of tumors.

2. Materials and methods

2.1. Synthesis of FeGd-HN

The FeGd-HN was synthesized according to a reported procedure [48]. Briefly, 40 mL of PAA solution (4.0 mg/mL) was first purged with nitrogen (≥50 min) to remove oxygen. After that, PAA solution was then heated to reflux. Then, 0.8 mL mixture of iron precursors (0.50 M $FeCl_3 \cdot 6H_2O$ plus 0.25 M $FeSO_4 \cdot 7H_2O$) was quickly injected into the heated polymer solution, followed by addition of 12 mL of ammonia solution (28%). Exceedingly small magnetic iron oxide nanoparticles (ES-MIONs) were then obtained after 30 min of reaction under magnetic stirring. After that, 0.70 mL of $Gd(NO_3)_3$ (0.50 M) and 6.0 mL of ammonia solution (28%) were added. The reaction was kept for another 90 min under magnetic stirring at 100 °C. Then, the solutions were cooled down to room temperature. The obtained FeGd-HN were purified by membrane dialysis (Mw cut-off 6000–8000 Da) against MilliQ water

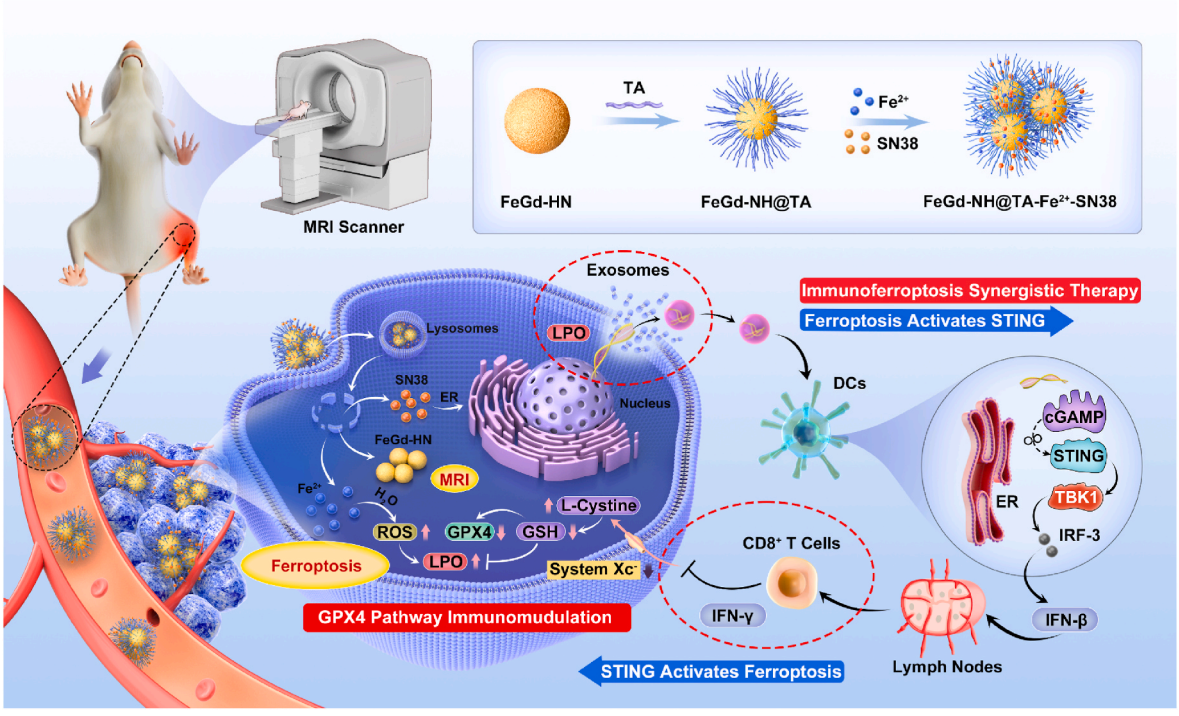

Scheme 1. Schematic illustration for the synthesis of FeGd-HN@TA-Fe^{2+}-SN38, and the principle of mutual activation of GPX4 and STING pathways for immunoferroptosis therapy.

for 5.0 days with a daily change of water. The purified FeGd-HN were collected and concentrated by a centrifugal ultrafiltration (Millipore, Mw cut-off 3000 Da). The Fe and Gd concentrations in the samples were measured by inductively coupled plasma-optical emission spectroscopy (ICP-OES, iCAP PRO, Thermo Fisher Scientific, US).

2.2. Synthesis of FeGd-HN@TA-Fe^{2+}

2.5 mL of FeGd-HN (C_{Fe} = 2.45 mM; C_{Gd} = 7.56 mM) and 100 μL of TA (10.0 mg/mL) aqueous solutions were added into 17.5 mL of pure water. After stirring for 30 min at room temperature, 800-200 μL of Fe^{2+}

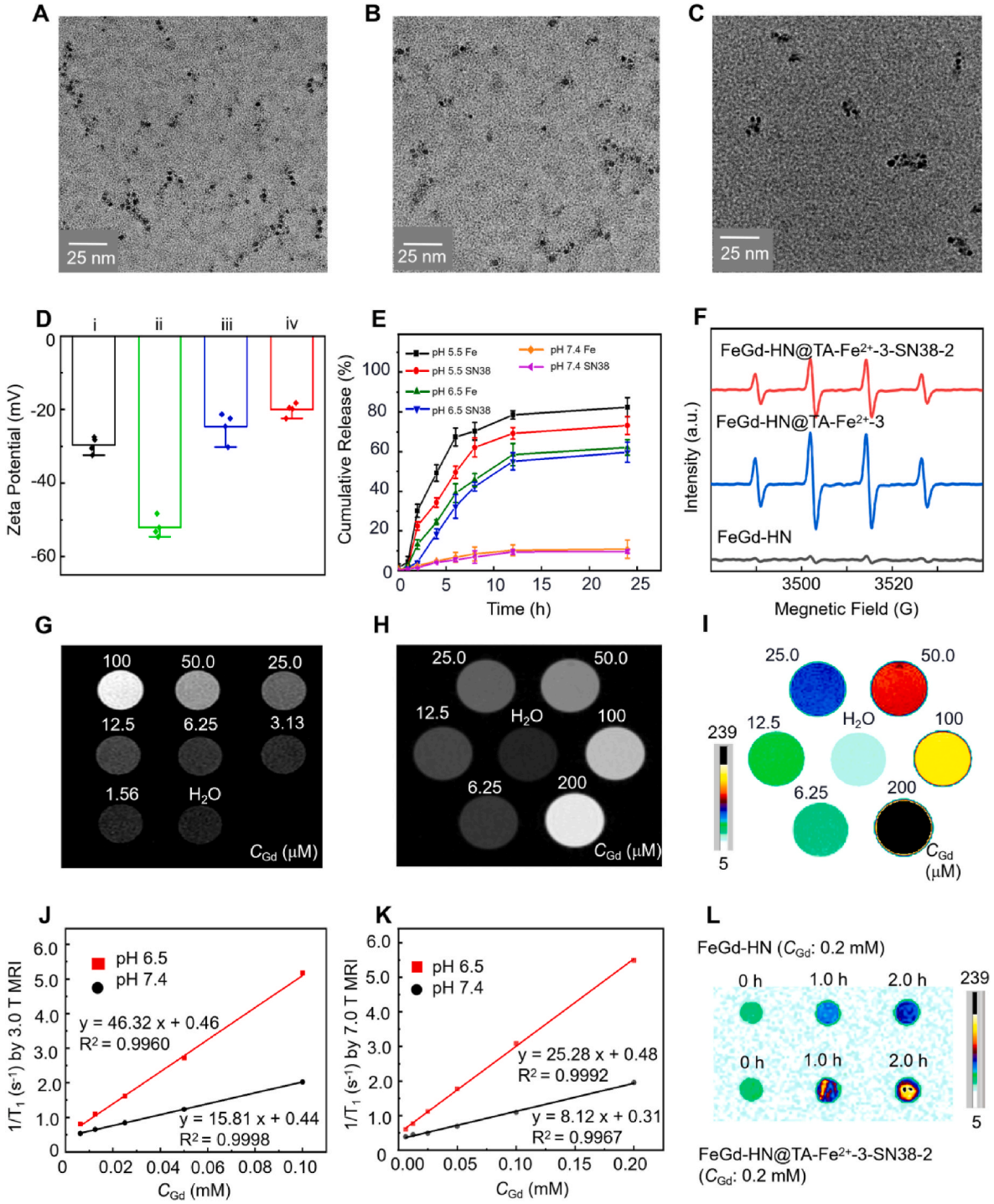

Fig. 1. (A–C): TEM images of FeGd-HN (A), FeGd-HN@TA-Fe^{2+}-3 (B) and FeGd-HN@TA-Fe^{2+}-3-SN38-2 (C). (D): Zeta potential of FeGd-HN (i), FeGd-HN@TA (ii), FeGd-HN@TA-Fe^{2+}-3 (iii), and FeGd-HN@TA-Fe^{2+}-3-SN38-2 (iv). (E): Fe and SN38 cumulative release curves of FeGd-HN@TA-Fe^{2+}-3-SN38-2 at pH 7.4, 6.5, or 5.5. (F): ESR measurements for FeGd-HN, FeGd-HN@TA-Fe^{2+}-3, and FeGd-HN@TA-Fe^{2+}-3-SN38-2 incubated at pH 6.5 with H_2O_2 (100 μM) for 6.0 h. (G): T_1-weighted MR image of FeGd-HN@TA-Fe^{2+}-3-SN38-2 with various C_{Gd} observed by a 3.0 T clinical MRI system (TE = 400 ms, TR = 7.30 ms). (H, I): The black & white (I) and corresponding pseudo-color (J) of T_1-weighted MR images for FeGd-HN@TA-Fe^{2+}-3-SN38-2 with various C_{Gd} observed by a 7.0 T MRI scanner (TE = 200 ms, TR = 6.30 ms) as incubated at pH 6.5 for 12 h. (J, K): T_1 relaxation rate ($1/T_1$) observed by a 3.0 T (K), or 7.0 T (L) of MRI scanner plotted as a function of C_{Gd} for FeGd-HN@TA-Fe^{2+}-3-SN38-2 incubated at pH 7.4 or 6.5 for 12 h. (L): Pseudo-color T_1-weighted MR images of 4T1 cells treated with FeGd-HN (C_{Gd} = 0.2 mM) or FeGd-HN@TA-Fe^{2+}-3-SN38-2 (C_{Gd} = 0.2 mM) for 0, 1.0, or 2.0 h.

($FeSO_4{\cdot}7H_2O$, 38 μM) aqueous solutions were added to the above FeGd-HN@TA solutions. After 30 min of reaction under magnetic stirring at room temperature, FeGd-HN@TA-Fe^{2+} (dark blue solutions) were obtained, and then purified by dialysis (Mw cut-off 3000 Da) to remove free Fe^{2+} and TA.

2.3. Synthesis of FeGd-HN@TA-Fe^{2+}-SN38

2.5 mL of FeGd-HN (C_{Fe} = 2.45 mM; C_{Gd} = 7.56 mM) and 100 μL of TA (10 mg/mL) aqueous solutions were added into 17.5 mL of pure water. After stirring for 30 min at room temperature, 200 μL of Fe^{2+} (38 μM) and 10–40 μL of SN38 (2.5 mM) in DMSO solutions were mixed and the mixtures were respectively added into the above FeGd-HN@TA solution. After further 30 min of reaction under magnetic stirring at room temperature, FeGd-HN@TA-Fe^{2+}/SN38 was obtained and then purified by dialysis (Mw cut-off 3000 Da) to remove free Fe^{2+} and SN38.

3. Results and discussion

3.1. Synthesis and characterization of FeGd-HN@TA-Fe^{2+}-SN38

The FeGd-HN was first synthesized according to our previous reported procedures. The average particle size is measured to be 5.5 nm from the transmission electron microscopy (TEM) images (Fig. 1A), which is similar with our previous results [48]. Subsequently, the TA-Fe^{2+} complexion layer was chelated on the surface of FeGd-HN. The synthesis conditions and characterization results of FeGd-HN@TA-Fe^{2+}-1-3 are summarized in Table S1. The size distributions of FeGd-HN@TA-Fe^{2+}-1-3 measured by dynamic light scattering (DLS) exhibit with narrow peaks (Fig. S1). The hydrodynamic diameter (d_h) was measured to be 186.3 ± 10.7, 112.6 ± 12.4 nm, and 8.5 ± 3.2 nm for FeGd-HN@TA-Fe^{2+}-1-3, respectively. The very large d_h of FeGd-HN@TA-Fe^{2+}-1 and FeGd-HN@TA-Fe^{2+}-2 indicates the aggregation of the nanoparticles. Therefore, FeGd-HN@TA-Fe^{2+}-3 is the optimal sample due to its ideal d_h and good dispersibility in water. The size of FeGd-HN@TA-Fe^{2+} increases with the iron addition amount, which could be attributed to the growth of the metal polyphenol network of TA-Fe^{2+}.

The synthesis conditions and characterization results of FeGd-HN@TA-Fe^{2+}-3-SN38-1-3 are shown in Table S2. Since the nanoparticles size is crucial for its accumulation at tumor location and the half-time in blood circulation [49,50], the hydrodynamic size d_h was measured by DLS (Fig. S2). Because the FeGd-HN@TA-Fe^{2+}-SN38 is utilized as a MRI CA for tumor theranostics, a smaller size with a high loading content of Fe^{2+} and SN38 is the ideal choice. FeGd-HN@TA--Fe^{2+}-3-SN38-3 with the d_h of 17.9 ± 3.6 nm and FeGd-HN@TA--Fe^{2+}-3-SN38-2 with d_h of 27.2 ± 4.5 nm could be better choices than FeGd-HN@TA-Fe^{2+}-3-SN38-1 with the d_h of 136.5 ± 6.6 nm. FeGd-HN@TA-Fe^{2+}-3-SN38-2 is the optimal sample due to its higher SN38 loading content (14.54 ± 0.89%) than that of FeGd-HN@TA--Fe^{2+}-3-SN38-3 (5.76%). The Fe^{2+} loading content of FeGd-HN@TA--Fe^{2+}-3-SN38-2 was measured to be 10.93 ± 2.45% by ICP-OES. Fig. 1B and C respectively display the TEM images of the FeGd-HN@TA-Fe^{2+}-3 and FeGd-HN@TA-Fe^{2+}-3-SN38-2, showing a slight assembly of the nanoparticles, which is consistent with the above-mentioned DLS results.

Fig. 1D shows the zeta potential of the nanoparticles measured by DLS. Due to the coating of TA layer with negative charged carboxyl groups, the zeta potential of FeGd-HN@TA (−52.05 ± 2.7 mV) is much lower than that of FeGd-HN (−29.65 ± 2.2 mV). In addition, the zeta potential of FeGd-HN@TA-Fe^{2+}-3 and FeGd-HN@TA-Fe^{2+}-3-SN38-2 is respectively −24.6 ± 3.9 mV and −19.97 ± 1.75 mV, which are both much higher than that of FeGd-HN@TA due to the loading of positive charged Fe^{2+}. These results indicate the successful coating of TA layer and loading of Fe^{2+}.

Fig. S3 and Table S4 show the schematic illustration for the structure of FeGd-HN, FeGd-HN@TA-Fe^{2+}-3 and FeGd-HN@TA-Fe^{2+}-3-SN38-2, the related functional groups and vibrations of PAA, TA and SN38, and the Fourier transform infrared spectroscopy (FT-IR) spectra. The peaks of FeGd-HN, *i.e.*, 1460 cm^{-1} (the in-plane bending vibration of C–O of –COOH) and 1319 cm^{-1} (stretching vibration of C–O in –COOH), can be attributed to PAA [51], which is the stabilizer of FeGd-HN. For FeGd-HN@TA-Fe^{2+}-3, the peaks of 1450 cm^{-1} and 1310 cm^{-1} illustrate the existence of PAA, and the peaks of 1720 cm^{-1} (the stretching vibration of C═O), 1190, 1080, 1120 cm^{-1} (the C–*O*–C stretching vibration) and 765 cm^{-1} (the out-plane bending vibration of C–H in benzene) [51] indicate the successful binding of TA on FeGd-HN. For FeGd-HN@TA-Fe^{2+}-3-SN38, the peaks of 1460 cm^{-1} and 1310 cm^{-1} confirm the existence of PAA (FeGd-HN), the peaks of 1725 cm^{-1}, 1180 cm^{-1}, 1100 cm^{-1}, 1030 cm^{-1} and 765 cm^{-1} demonstrate the existence of TA, and the peaks of 1580 cm^{-1} (stretching vibration of C═O) and 1665 cm^{-1} (stretching vibration of C═N in amide) which are in accordance with the peaks of SN38 [52,53] illustrate the existence of TA-Fe^{2+}-SN38 layer on the surface of FeGd-HN, indicating the successful synthesis of FeGd-HN@TA-Fe^{2+}-3-SN38-2.

The ^1H NMR can further prove the existence of TA-Fe^{2+}-SN38 layer. Figs. S4–S7 show the ^1H NMR of SN38, TA, FeGd-HN@TA-Fe^{2+}-3-SN38-2 and FeGd-HN@TA-Fe^{2+}-3-SN38-2 with pH-responsiveness degradation. The active hydrogen signal from SN38 (δ 10.29 s, 1H, Fig. S4) and TA (δ 9.62, d, 9H, Fig. S5) cannot not been seen in the ^1H NMR of FeGd-HN@TA-Fe^{2+}-3-SN38-2 (Fig. S6). However, after degradation of FeGd-HN@TA-Fe^{2+}-3-SN38-2 under pH 6.8, the signal of active hydrogen appears (δ 9.0–10.6 (w, 35H), Fig. S7). This phenomenon could be attributed to the Fe–O bonding of Fe^{2+} with TA and SN38, which suggesting the existence of TA-Fe^{2+}-SN38 layer. As shown in Fig. S8, the complexing of TA and SN38 with Fe^{2+} is essential for the formulation of polyphenolic network structure, which possesses pH-responsive degradation to release SN38 and Fe^{2+} in tumor microenvironment (TME) for ferroptosis therapy.

Moreover, the X-ray photoelectron spectroscopy (XPS) spectra of FeGd-HN@TA-Fe^{2+}-3-SN38-2 and FeGd-HN can also prove the existence of TA-Fe^{2+}-SN38 layer from the N 1s peak and ratio of Fe^{2+}/Fe^{3+}. As shown in Fig. S9A, the peak of N1s (399.1 eV) as appeared in the XPS spectrum of FeGd-HN@TA-Fe^{2+}-3-SN38-2 suggests the SN38 existence. The valence state and Fe^{2+}/Fe^{3+} ratio analyzed by the curve fitting of $Fe2p_{1/2}$ and $Fe2p_{3/2}$, as shown in Figs. S9B and S9C, Table S5 and Table S6, indicate that the FeGd-HN@TA-Fe^{2+}-3-SN38-2 has a much higher Fe^{2+}/Fe^{3+} ratio (69.64:30.36) than that of FeGd-HN (34.24:65.76), which indicates the Fe^{2+} loading by the polyphenolic network structure.

The cumulative release behaviors of Fe (measured by ICP-OES) and SN38 (measured by the fluorescence calibration curve of SN38 in Fig. S10) at pH 5.5, pH 6.5 and pH 7.4 are shown in Fig. 1E. After 12 h of incubation, the cumulative release percentage of Fe and SN38 respectively reach 78.5 ± 2.1% and 69.2 ± 2.9% at pH 5.5, 58.5 ± 5.6% and 55.1 ± 4.3% at pH 6.5, but only 10.3 ± 2.5% of Fe and 9.7 ± 0.99% of SN38 at pH 7.4. These results indicate the effective release of Fe and SN38 from FeGd-HN@TA-Fe^{2+}-3-SN38-2 in the acidic of TME and endosome conditions, and the stability of FeGd-HN@TA-Fe^{2+}3-SN38-2 during the blood circulation [17,54].

The electron spin resonance (ESR) spectrum, which demonstrates the ROS generation ability of the nanoparticles, was also measured for FeGd-HN, FeGd-HN@TA-Fe^{2+}-3 and FeGd-HN@TA-Fe^{2+}-3-SN38-2 as shown in Fig. 1F. From the characteristic peaks of •OH (1:2:2:1 signal), it is observed that both FeGd-HN@TA-Fe^{2+}-3 and FeGd-HN@TA-Fe^{2+}-3-SN38-2 show much stronger signal of •OH than FeGd-HN. That's because the loaded Fe^{2+} can accelerate the Fenton reaction, producing •OH. Although the groups of FeGd-HN@TA-Fe^{2+}-3-SN38-2 and FeGd-HN@TA-Fe^{2+}-3 have the same concentration of Fe, the FeGd-HN@TA-Fe^{2+}-3 group exhibit with higher •OH signal than FeGd-HN@TA-Fe^{2+}-3-SN38-2 group, which could be attributed to the lipophilicity of SN38 that prevents the interaction between TA and Fe^{2+}.

From the T_1-weighted MR images of FeGd-HN@TA-Fe^{2+}-3-SN38-2 with various C_{Gd} observed by a 3.0 T clinical MRI system (Fig. 1G) or by a 7.0 T MRI scanner (Fig. 1H and I), it is obvious that the T_1 signal depends on the Gd concentration, which demonstrates that FeGd-HN@TA-Fe^{2+}-3-SN38-2 can be used as a T_1-weighted MRI CA.

The T_1 relaxiation rate ($1/T_1$) (Fig. 1J and K; Figs. S11A–D) and T_2 relaxiation rate ($1/T_2$) (Figs. S12A–F) of FeGd-HN@TA-Fe^{2+}-3-SN38-2 (3 batches) with various C_{Gd} measured at 3.0 or 7.0 T scanner are plotted as a function of C_{Gd}, from which the slopes of linear lines are considered as r_1 and r_2. Because the r_2/r_1 ratio is also significant for the T_1-weighted MR imaging performance evaluation [48,55,56], the r_1, r_2 values and r_2/r_1 ratios of FeGd-HN@TA-Fe^{2+}-3-SN38-2 measured at 3.0 or 7.0 T are summarized in Table S3. After 12 h of incubation at pH 7.4, the FeGd-HN@TA-Fe^{2+}-3-SN38-2 exhibits a relatively low r_1 value (16.10 $\pm$ 2.50 at 3.0 T; 8.05 $\pm$ 0.17 at 7.0 T) and a relatively high r_2/r_1 ratio (9.45 $\pm$ 2.35 at 3.0 T; 19.44 $\pm$ 1.03 at 7.0 T), which is not advantageous for the T_1-weighted MRI. However, after 12 h of incubation at pH 6.5, the FeGd-HN@TA-Fe^{2+}-3-SN38-2 presents a very high r_1 value (46.79 $\pm$ 0.41 at 3.0 T; 25.10 $\pm$ 1.24 at 7.0 T) and a very low r_2/r_1 ratio (1.67 $\pm$ 0.05 at 3.0 T; 1.53 $\pm$ 0.14 at 7.0 T), which is extremely favorable for the T_1-weighted MRI. These results suggest that the slight acidic TME (pH $\sim$ 6.5) results in shedding of the TA-Fe^{2+}-SN38 complexing layer, and the exposed FeGd-HN exhibits remarkable MRI performance.

Fig. 1L shows the Pseudo-color T_1-weighted MR images of 4T1 cells treated with FeGd-HN (C_{Gd} = 0.2 mM) or FeGd-HN@TA-Fe^{2+}-3-SN38-2 (C_{Gd} = 0.2 mM) for 0 h, 1.0 h, or 2.0 h. It is found that the T_1 signal of the cells increases with increasing the incubation time, and FeGd-HN@TA-Fe^{2+}-3-SN38-2 exhibits a better MRI performance than the FeGd-HN because the nanoparticles with TA coating exhibits with higher cellular uptake due to the nanoparticle-cell interactions. The released TA from FeGd-HN@TA-Fe^{2+}-3-SN38-2 could be removed from the body *via* renal excretion [57]. Therefore, FeGd-HN@TA-Fe^{2+}-3-SN38-2 is a potential T_1-weighted CA to be used for MRI-guided tumor therapy.

3.2. Cellular uptake and endo/lysosome escape of FeGd-HN@TA-Fe^{2+}-SN38

Fig. S13 shows the CLSM images of 4T1 cells treated by DMEM medium without (control) or with SN38, FeGd-HN@TA-Fe^{2+}-3, or FeGd-HN@TA-Fe^{2+}-3-SN38-2. The treated 4T1 cells were stained by DAPI (cells nuclei, blue), FITC-actin (cell cytoskeletons, green) and FeRhoNox-1 (intracellular Fe^{2+}, red). It is found that both FeGd-HN@TA-Fe^{2+}-3 and FeGd-HN@TA-Fe^{2+}-3-SN38-2 groups exhibit strong FeRhoNox-1 signals inside the cells compared with the control and SN38 groups, which indicates the high cellular uptake of the nanoparticles.

Figs. S14A and B shows the fluorescence distributions and the corresponding qualification results as measured by flow cytometry (FC) of the cells treated by DMEM medium without (control) or with SN38, FeGd-HN@TA-Fe^{2+}-3, or FeGd-HN@TA-Fe^{2+}-3-SN38-2. It is observed that both FeGd-HN@TA-Fe^{2+}-3 and FeGd-HN@TA-Fe^{2+}-3-SN38-2 groups exhibit obvious intracellular Fe^{2+} level increase compared with the control and SN38 groups, which reinforces the high cellular uptake of the nanoparticles concluded from the CLSM results. Regarding the stability of Fe^{2+}, TA exhibits with reductive properties which can prevent Fe^{2+} from being oxidized to Fe^{3+}. The Fe^{2+} can be protected in the complexing layer of TA-Fe^{2+}-SN38 on the surface of FeGd-HN during the blood circulation. Moreover, the cumulative release of the Fe (Fig. 1E) suggests the stability of FeGd-HN@TA-Fe^{2+}-SN38 under pH 7.4. In addition, the intracellular Fe^{2+} detected by CLSM (Fig. S13) and flow cytometry (Fig. S14) demonstrates the stability of released Fe^{2+} in tumor cells.

Cellular uptake of SN38 with green fluorescence [57] measured by flow cytometry is shown in Fig. S15A (the fluorescence distribution), and Fig. S15B (the corresponding qualification results). It is obvious that the FeGd-HN@TA-Fe^{2+}-3-SN38-2 treated 4T1 cells has even higher intracellular SN38 level than the SN38 treated 4T1 cells, which could be attributed to the enhancement of cellular uptake and pH-responsiveness of TA-Fe^{2+}-SN38 layers.

Fig. S16 shows the CLSM images of 4T1 cells treated by DMEM medium without (control) or with SN38, FeGd-HN@TA-Fe^{2+}-3 or FeGd-HN@TA-Fe^{2+}-3-SN38-2, and stained with DAPI (cells nuclei, blue), Endo/lyso-Tracker Green (endo/lysosomes, green), and FeRhoNox-1 (intracellular Fe^{2+}, red). Lots of red dots can be found in the cells without overlap with green dots for the FeGd-HN@TA-Fe^{2+}-3 and FeGd-HN@TA-Fe^{2+}-3-SN38-2 groups, which demonstrates the endo/lysosome escape of the released Fe^{2+} from FeGd-HN@TA-Fe^{2+}-3 and FeGd-HN@TA-Fe^{2+}-3-SN38-2, and the potential of FeGd-HN@TA-Fe^{2+}-3 and FeGd-HN@TA-Fe^{2+}-3-SN38-2 to be used for tumor ferroptosis therapy *via* enhancing intracellular Fe^{2+} level.

3.3. FeGd-HN@TA-Fe^{2+}-SN38 mediated ferroptosis therapy and its mechanism

The DCFH-DA was utilized to stain the 4T1 cells to specifically identify the generation of intracellular ROS, which induces ferroptosis. Fig. S17 shows the CLSM images of the 4T1 cells treated by DMEM medium without (control) or with SN38, FeGd-HN@TA-Fe^{2+}-3 or FeGd-HN@TA-Fe^{2+}-3-SN38-2, and stained with DCFH-DA (green). Both FeGd-HN@TA-Fe^{2+}-3 and FeGd-HN@TA-Fe^{2+}-3-SN38-2 groups present robust green dots, indicating the increase of intracellular ROS level. Moreover, the green fluorescence distribution of the treated 4T1 cells determined by FC and the corresponding quantification results are shown in Figs. S18A and B. Compared with the control and SN38 groups, the FeGd-HN@TA-Fe^{2+}-3 and FeGd-HN@TA-Fe^{2+}-3-SN38-2 groups show much stronger green fluorescence ($p < 0.001$). Therefore, our FeGd-HN@TA-Fe^{2+}-3 and FeGd-HN@TA-Fe^{2+}-3-SN38-2 are promising to be used for tumor ferroptosis therapy *via* generation of robust ROS induced by the high level of intracellular Fe^{2+}, which reacts with the intracellular H_2O_2 based on the Fenton reaction.

Fig. S19 shows the CLSM images of the 4T1 cells treated by DMEM medium without (control) or with SN38, FeGd-HN@TA-Fe^{2+}-3 or FeGd-HN@TA-Fe^{2+}-3-SN38-2, and stained with DAPI (cells nuclei, blue) and BODIPY C11-581/591 (intracellular LPO, green), which is LPO-specific probe with red fluorescence at the reductive state and green fluorescence at the oxidative state. Compared with the control and SN38 groups, both FeGd-HN@TA-Fe^{2+}-3 and FeGd-HN@TA-Fe^{2+}-3-SN38-2 groups present enhanced green fluorescence and attenuated red fluorescence, indicating the intracellular LPO accumulation. In addition, the red fluorescence distribution of the treated 4T1 cells with staining of BODIPY C11-581/591 determined by FC, and the corresponding quantification results are shown in Figs. S20A and B. The significant decrease of the red fluorescence is found for both FeGd-HN@TA-Fe^{2+}-3 and FeGd-HN@TA-Fe^{2+}-3-SN38-2 groups comparing with the control and SN38 groups, which reinforces the high accumulation of intracellular LPO.

To further verify the cell death induced by FeGd-HN@TA-Fe^{2+}-3-SN38-2 is ferroptosis, inhibitors of ferroptosis were utilized in our studies, including Fer-1 and DFO that can eliminate the intracellular Fe^{2+} [58], L-cystine that is necessary for intracellular GSH synthesis, GSH that is the substrate of GPX4 [59], N-acetyl-L-cysteine (NAC) that is a ROS scavenger [60], Vitamin E (V_E) that can decrease the level of intracellular H_2O_2 [61]. The ROS generation of the treated cells with addition of ferroptosis inhibitors, *i.e.*, Fer-1 (2.0 μM), DFO (100 μM), L-cystine (2.0 mM), GSH (2.0 mM), NAC (2.0 mM), V_E (25 mM), were determined by DCFH-DA assay and FC. The green fluorescence distributions (Fig. S21A) and the corresponding quantification results (Fig. S21B) indicate the significant intracellular ROS suppression by the above-mentioned ferroptosis inhibitors ($p < 0.0001$). This result demonstrates that the decreasing of intracellular Fe^{2+}/Fe^{3+} concentration by Fer-1 or DFO, the activation of GPX4 activity by GSH or L-cystine, the scavenging of intracellular ROS by NAC, and the depletion of intracellular H_2O_2 by V_E can prevent the ROS generation, which reinforce the

existence of ferroptosis in cancer cells introduced by FeGd-HN@TA-Fe^{2+}-3-SN38-2.

The intracellular LPO accumulation with addition of ferroptosis inhibitors were also determined by FC. The treated 4T1 cells were stained with BOIDPY C11-581/591 to determine the intracellular LPO level. Figs. S22A and B show the green fluorescence distributions and the corresponding quantification results. It is obvious that the ferroptosis inhibitors, including Fer-1, DFO, L-cystine, GSH, NAC and V_E, can inhibit the LPO accumulation. These results reinforce the critical role of FeGd-HN@TA-Fe^{2+}-3-SN38-2 on ferroptosis inducing in cancer cells.

Fig. S23 shows GPX4 levels in the 4T1 cells measured by ELISA kits after various treatments. The 4T1 cells treated with FeGd-HN@TA-Fe^{2+}-3 and FeGd-HN@TA-Fe^{2+}-3-SN38-2 exhibit obvious decreased GPX4 level, compared with the control and SN38 groups. However, the GPX4 level in the cells treated with FeGd-HN@TA-Fe^{2+}-3-SN38-2 with addition of Fer-1 or L-cystine exhibits significant recovery. From Fig. S24, it is found that the intracellular level of GSH (an important substrate of GPX4) in the 4T1 cells treated with FeGd-HN@TA-Fe^{2+}-3 or FeGd-HN@TA-Fe^{2+}-3-SN38-2 also significantly decreases, compared with the control and SN38 groups. Similarly, the GSH level in the cells treated with FeGd-HN@TA-Fe^{2+}-3-SN38-2 with addition of Fer-1 or L-cystine is comparable to that of the control and SN38 groups, which is in accordance with the above-mentioned GPX4 assay results. Therefore, it can be concluded that FeGd-HN@TA-Fe^{2+}-3-SN38-2 can be utilized for ferroptosis therapy of tumors.

The cells viabilities tested by MTT assay, as shown in Fig. S25, demonstrate the killing effect of FeGd-HN@TA-Fe^{2+}-3-SN38-2 on the cancer cells. Moreover, the addition of the ferroptosis inhibitors, *i.e.*, Fer-1, GSH and NAC, can largely increase the cell viability of cancer cells, which demonstrates the effectiveness of FT provoked by FeGd-HN@TA-Fe^{2+}-3-SN38-2.

3.4. *FeGd-HN@TA-Fe^{2+}-SN38 mediated immunotherapy and its mechanism*

According to the mechanism of the STING pathway activation *via* SN38 [42], it is hypothesized that the released SN38 from FeGd-HN@TA-Fe^{2+}-3-SN38-2 in cancer cells leads to exocytosis of DNA contained exosomes from the cancer cells.

As shown in Fig. 2A, it could be found that the synergy effect from ferroptosis and SN38 in FeGd-HN@TA-Fe^{2+}-3-SN38-2 group has obvious DNA damage on 4T1 cells. The related apoptosis of the treated 4T1 cells could be seen in Fig. S26. As shown in Fig. 2B, the colocalization of the dsDNA (stained by green Picogreen) and CD63 (the specific biomarker of exosomes, stained by red immunofluorescence) indicates that the DNA fragments containing exosomes are generated. The high intensity of dsDNA and CD63 in group iv suggests that the synergistic effect from SN38 and ferroptosis together promotes the DNA fragments containing exosomes generation. The cells membranes staining by Dio as shown in Fig. 2C reveals the cells membrane damage by LPO when ferroptosis happens. As shown in Fig. 2D, the dsDNA of the cancer cells stained by Picogreen and uptaken by BMDCs, as detected by direct adding the culture medium (CM) of 4T1 cells to DCs, demonstrate that the FeGd-HN@TA-Fe^{2+}-3-SN38-2 treated cancer cells can delivery robust DNA fragments to BMDCs. Therefore, it could be concluded that ferroptosis promotes DNA-fragments delivery to BMDCs by the fierce DNA damages due to the ROS generation and intense exosomes exocytosis due to the cancer cells membranes damage by LPO accumulation.

Moreover, to explore why ferroptosis provokes exosomes generation from 4T1 cells, investigations were taken by CLSM observation of lipid droplets, LPO accumulation, expression of Rab8a, Plin5 and CD63. As a biomarker of exosomes generation from cells, the CD63 could be upregulated by Rab8a [62]. The lipid droplets, an organelle for storage of the unsaturated fatty, are reported to have a strong linkage with mitochondrion by Rab8a and Plin5 [63,64]. With the happening of ferroptosis in cells, the lipid droplets increased, as revealed by Fig. S27. The 4T1 cells treated by FeGd-HN@TA-Fe^{2+}-3 (ii) and FeGd-HN@TA--Fe^{2+}-3-SN38-2 (iv) exhibits both increased signal of Lipi-Blue and decreased signal of reductive BODIPY C11-581/591. The high expression of adipose triglyceride lipase (ATGL) in groups of FeGd-HN@TA-Fe^{2+}-3 (ii) and FeGd-HN@TA-Fe^{2+}-3-SN38-2 (iv) measured by ELISA kits (Fig. S28), which is the biosynthetic enzyme for fatty acid esters of hydroxy fatty acids [65], is in accordance with the high expression of lipid droplets. The colocalization of the lipid droplets (Lipi-Blue) and mitochondrion (Mito-tracker Red), as shown in Fig. S29, indicates the migration of lipid droplets to mitochondrion, which could be considered as the way of cancer cells to relieve the stress of ferroptosis to mitochondrion. High expression of Rab8a and Plin5 stained by immunofluorescence (Figs. S29 and S30) confirms the specific linkage of lipid droplets to mitochondrion. The expression of CD63 is upregulated in 4T1 cells treated by FeGd-HN@TA-Fe^{2+}-3 (ii) and FeGd-HN@TA--Fe^{2+}-3-SN38-2 (iv) (Fig. S31). Therefore, the synergy effect of ferroptosis induced by FeGd-HN@TA-Fe^{2+}-SN38 in generation of DNA containing exosomes could be generalized below (Fig. S32): the released Fe^{2+} provokes ferroptosis by LPO accumulation, followed by the damage of cancer cells membrane and CD63 upregulation due to the lipid droplets activation; meanwhile, the released SN38 causes damage of DNA. All these provokes the DNA-fragments containing exosomes generation and excretion from treated cancer cells for activation of immunotherapy.

Fig. 2E schematically illustrates the progress of exosomes and DNA isolation from the supernatant of 4T1 cells treated by SN38, FeGd-HN@TA-Fe^{2+}-3, or FeGd-HN@TA-Fe^{2+}-3-SN38-2 with or without ferroptosis inhibitors. As shown in Fig. 2F, the relative exosomes content in the supernatant of FeGd-HN@TA-Fe^{2+}-3-SN38-2 treated 4T1 cells (group iv) is much higher than that of control (group i), and SN38 (group ii). However, with the addition of inhibitors of ferroptosis, FeGd-HN@TA-Fe^{2+}-3-SN38-2 + Fer-1 (group v) and FeGd-HN@TA-Fe^{2+}-3-SN38-2 + L-cystine (group vi) exhibit with obvious decrease of exosomes content, indicating that the ferroptosis in 4T1 cells can accelerate the exosomes secretion. The relative DNA content of SN38 group (ii) or FeGd-HN@TA-Fe^{2+}-3-SN38-2 group (iv) is respectively much higher than that of control group (i) or FeGd-HN@TA-Fe^{2+}-3 group (iii), which demonstrates that the SN38 and SN38-loaded nanoparticles can promote DNA disruption and then enhance the DNA content in the exosomes, as shown in Fig. 2G. In addition, with addition of ferroptosis inhibitors, *i.e.*, Fer-1 and L-cystine, the relative DNA content also significantly decreases, which illustrates that the ferroptosis can also promote the DNA exocytosis. Fig. 2H illustrates the mechanism why the ferroptosis can promote the exocytosis of DNA-containing exosomes. That's because the accumulation of LPO during ferroptosis disrupt the integrity of cells membrane.

Fig. 3A shows the STING pathway activation of the BMDCs by double strand (ds)-DNA from exosomes of cancer cells. Fig. 3B illustrates the BMDCs activation *via* STING pathway by CM of the 4T1 cells that may include dsDNA-containing exosomes, enhancing the expression of STING and IRF3 proteins in the BMDCs, and the exocytosis of cell cytokines IFN-β and IL-6. As shown in Fig. 3C, the high expression of p-STING, *p*-IRF3, IRF3, TBK1 and *p*-TBK1 evaluated by the western blotting (WB) assay demonstrates the STING pathway activation of the BMCDs after incubation with CM of 4T1 cells treated with FeGd-HN@TA-Fe^{2+}-3-SN38-2.

Fig. 3D shows the analysis of BMDCs maturation by as analyzed by anti-CD80 and anti-CD86. It is found that CM from SN38 (group ii) or FeGd-HN@TA-Fe^{2+}-3 (group iii) treated 4T1 cells can obviously promote BMDCs maturation compared with the control (group i). The former is because SN38 can induce DNA disruption and then enhance the DNA content in the exosomes, which can promote BMDCs maturation. The latter is because the immunogenic cell death (ICD) from the cancer cell fragments generated by ROS (*i.e.*, ferroptosis) induced by FeGd-HN@TA-Fe^{2+}-3 can also promote the BMDCs maturation [13,66,67]. In addition, it can be seen that the BMDCs maturation in the

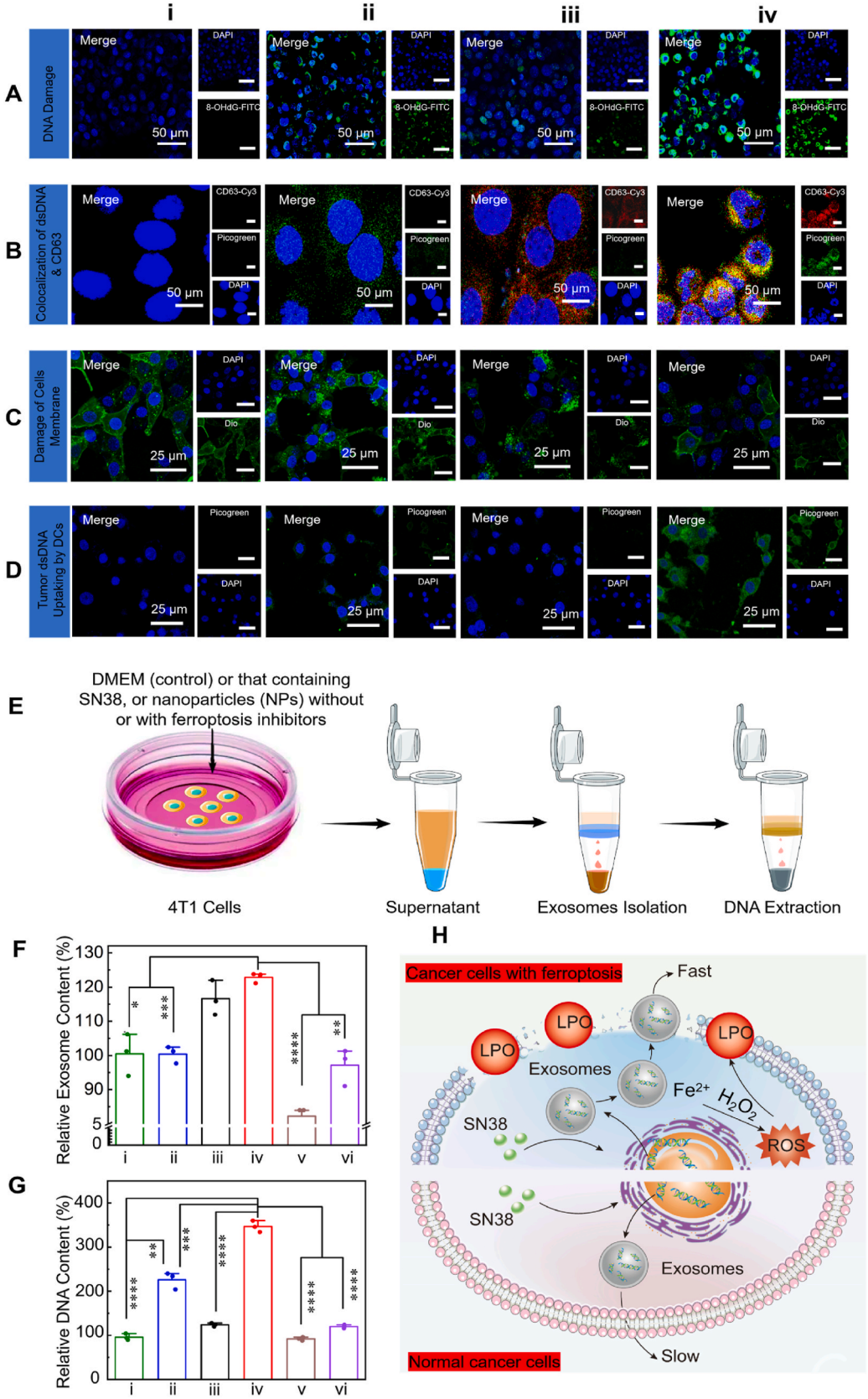

Fig. 2. (A–C): CLSM images of the 4T1 cells treated with (i) PBS (control), (ii) SN38, (iii) FeGd-HN@TA-Fe^{2+}-3, (iv) FeGd-HN@TA-Fe^{2+}-3-SN38-2, and stained with DAPI, rabbit anti-mouse 8-OHdG and goat anti-rabbit lgG H&L-FITC (A); or stained with DAPI, Picogreen, rabbit anti-mouse anti-CD63, and goat anti-rabbit lgG H&L-Cy3 (B); or with DAPI and Dio (C). (D): The BMDCs treated by the conditioned medium of the Picogreen stained 4T1 cell with treatment of i-iv, and stained with DAPI. (E): Schematic illustration for the isolation of exosomes and DNA from the supernatant of 4T1 cells treated with DMEM (control) or that containing SN38, or nanoparticles (NPs) without or with ferroptosis inhibitors. (F, G): Relative content of exosomes (F) or DNA (G) in the supernatants of 4T1 cells, which were treated with (i) control, (ii) SN38, (iii) FeGd-HN@TA-Fe^{2+}-3, (iv) FeGd-HN@TA-Fe^{2+}-3-SN38-2, (v) FeGd-HN@TA-Fe^{2+}-3-SN38-2 + Fer-1 (2.0 μM), or (vi) FeGd-HN@TA-Fe^{2+}-3-SN38-2 + L-cystine (2.0 mM). (H): Schematic illustration of exosomes exocytosis from cancer cells with or without ferroptosis. Mean ± SD, *P < 0.05, **P < 0.01, ***P < 0.001, ****P < 0.0001.

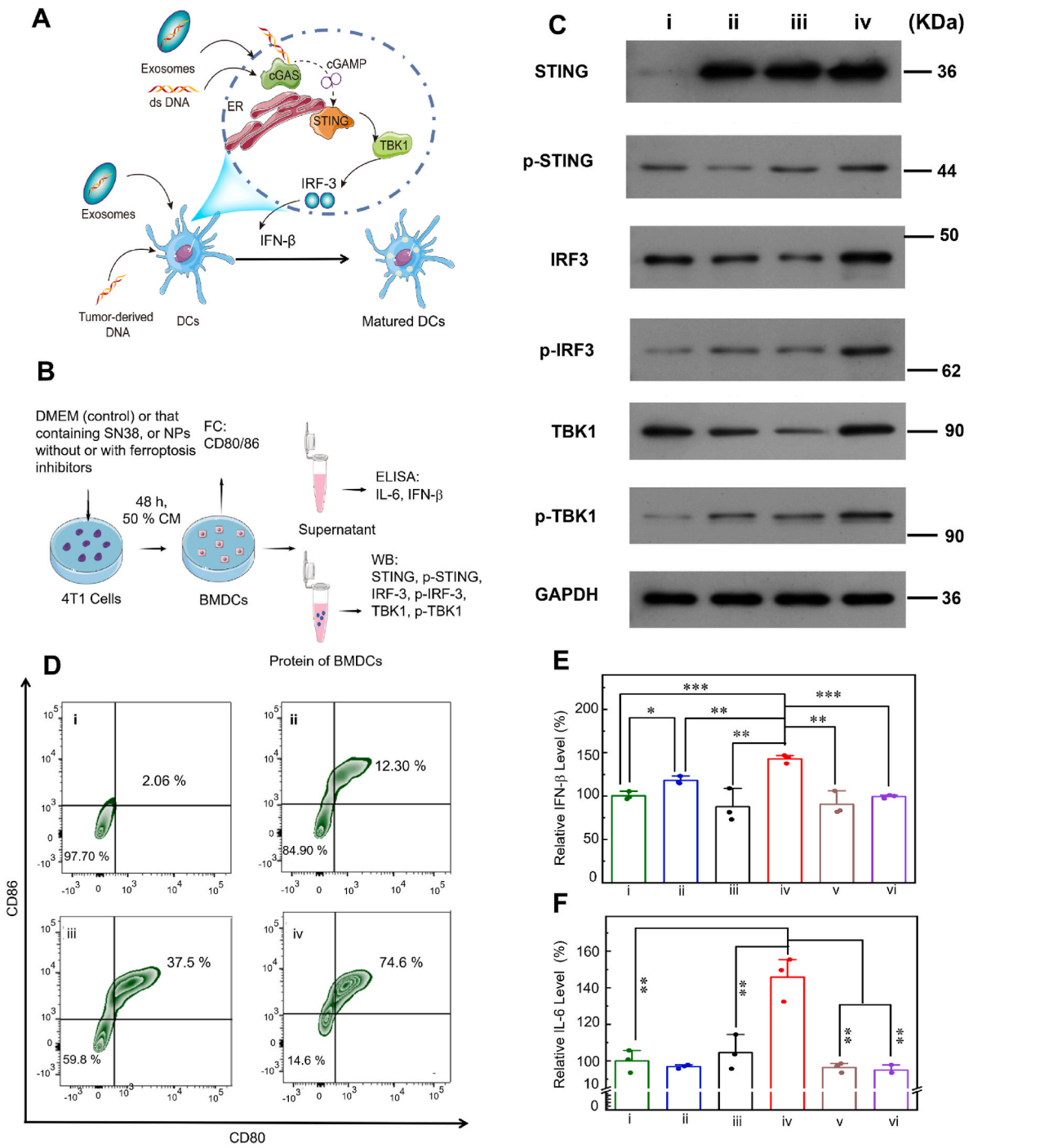

Fig. 3. (A): Schematic illustration for the STING pathway activation of the BMDCs by ds-DNA from exosomes of cancer cells. (B): Schematic illustration for BMDCs activation *via* STING pathway by CM of 4T1 cells, *i.e.*, DMEM (control) or that containing SN38, or NPs without or with ferroptosis inhibitors, enhancing the expression of STING pathway related proteins in the BMDCs, and the exocytosis of IFN-β and IL-6. (C) Western blot (WB) assay showing the expression of STING, p-STING, IRF3, *p*-IRF3, TBK1 and *p*-TBK1 protein in the BMCDs treated with the CM of 4T1 cells after incubation with (i) PBS (control), (ii) SN38, (iii) FeGd-HN@TA-Fe^{2+}-3 and (iv) FeGd-HN@TA-Fe^{2+}-3-SN38-2. (D) BMDCs maturation as detected by FC with staining of anti-CD80 and anti-CD86. (E, F): IFN-β (E) and IL-6 (F) levels in the supernatants of BMCDs with different treatment of 50% CM (i-vi), analyzed by ELISA kits. Mean ± SD, *P < 0.05, **P < 0.01, ***P < 0.001, ****P < 0.0001.

FeGd-HN@TA-Fe^{2+}-3-SN38-2 group (iv) is much higher than that of the SN38 group (ii) plus FeGd-HN@TA-Fe^{2+}-3 group (iii), displaying "1 + 1>2" of synergistic effects in BMDCs activation. Therefore, it can be concluded that FeGd-HN@TA-Fe^{2+}-3-SN38-2 can be utilized for immunoferroptosis synergistic therapy of tumors.

The exocytosis of cell cytokines IFN-β (Fig. 3E) and IL-6 (Fig. 3F) in the group FeGd-HN@TA-Fe^{2+}-3-SN38-2 (iv) are much higher than that of the group SN38 (ii) and FeGd-HN@TA-Fe^{2+}-3 (iii). However, with addition of ferroptosis inhibitors, the group of FeGd-HN@TA-Fe^{2+}-3-SN38-2 + Fer-1 (v) and FeGd-HN@TA-Fe^{2+}-3-SN38-2 + L-cystine (vi), exhibit much lower cytokines level of IFN-β and IL-6. These results demonstrate that the ferroptosis can significantly provoke enhanced STING activation in BMDCs *via* promoting the exocytosis of ds-DNA-containing exosomes.

3.5. *In vivo* behaviors of FeGd-HN@TA-Fe^{2+}-SN38 on tumor-bearing mice

The pharmacokinetic profile of Fe level in the 4T1 tumor-bearing BALB/c mice with intravenous injection of FeGd-HN@TA-Fe^{2+}-3-SN38-2 is shown in Fig. S33, from which the half-life time ($t_{1/2}$) in the blood stream is measured to be 2.41 h. The short $t_{1/2}$ can be ascribed to the small d_h of FeGd-HN@TA-Fe^{2+}-3-SN38-2 (*i.e.*, 27.2 ± 4.5 nm).

Fig. S34 shows the *in vivo* biodistribution of Fe level in the 4T1 tumor-bearing BALB/c mice with intravenous injection of FeGd-HN@TA-Fe^{2+}-3-SN38-2. The FeGd-HN@TA-Fe^{2+}-3-SN38-2 accumulates at tumor location due to the EPR effect, reaching 11.9 ± 3.47% I.D./g at 4.0 h post-injection. The accumulation in the liver and spleen could be mainly attributed to mononuclear phagocyte system (MPS), and that in the kidney is caused by the renal clearance of FeGd-HN (5.5 nm) degraded from FeGd-HN@TA-Fe^{2+}-3-SN38-2 under TME.

Fig. 4A shows the axial T_1-weighted MR images of 4T1 tumor-bearing mice at predetermined time points after *i.v.* injection of FeGd-HN@TA-Fe^{2+}-3-SN38-2 or the commercially available Magnevist. The MRI signal of tumors is strongest at 4.0 h post-injection of FeGd-HN@TA-Fe^{2+}-3-SN38-2, which is consistent with the above-mentioned results of pharmacokinetic and biodistribution studies. However, the strongest MRI signal of tumors at 10 min post-injection of the Magnevist (control) is much weaker than that of the FeGd-HN@TA-Fe^{2+}-3-SN38-2 because the Magnevist is a small molecule with a molecular weight of 938.0 Da.

The corresponding quantitative analysis of the MRI signal of tumors is shown in Fig. 4B and C utilizing ΔSNR, according to Equations (1) and (2) [48,55,68,69].

$$SNR = \frac{SI\ mean}{SD\ noise} \tag{1}$$

$$\Delta SNR = \frac{SNRpost - SNRpre}{SNRpre} \times 100\ \% \tag{2}$$

The highest ΔSNR of the FeGd-HN@TA-Fe^{2+}-3-SN38-2 group at 4.0 h is 167.3 ± 5.0% (Fig. 4B), which is much higher ($p < 0.0001$) than that of the Magnevist group at 10 min (*i.e.*, 71.2 ± 4.6%, Fig. 4C). The remarkable *in vivo* MRI performance of the FeGd-HN@TA-Fe^{2+}-3-SN38-2 could be attributed to its high accumulation at tumor location, the high relaxivities of FeGd-HN core, and the pH-sensitive TA-Fe^{2+}-SN38 layer that could be degraded in TME.

The *in vivo* tumor inhibition experiments (Fig. 5A) were evaluated on the 4T1 tumor-bearing mice after intravenous injection of PBS (control, group i), αPD-L1 (group ii), SN38 (group iii), FeGd-HN@TA-Fe^{2+}-3 (group iv), FeGd-HN@TA-Fe^{2+}-3-SN38-2 (v) and FeGd-HN@TA-Fe^{2+}-3-SN38-2 + αPD-L1 (group vi). The combination of αPD-L1 was used for *in vivo* tumor therapy because αPD-L1 can upregulate the activity of $CD8^+$ T cells, which can further inhibit the bioactivity of system X_c^-, resulting in lower intracellular L-cystine level and downregulation of GPX4 that benefits the efficacy of ferroptosis therapy [70–73].

Fig. 5B and C shows the 1st tumor growth curves and the corresponding percentage survival, respectively. In the group i (PBS, control), the tumors grow exponentially with one mouse euthanized at day 16 post-injection due to its excessive tumor size (>2000 mm^3). The αPD-L1 (group ii) and SN38 (group iii) exhibit slight inhibition of the tumor growth with mice euthanized at day 24 and 26, respectively. FeGd-HN@TA-Fe^{2+}-3 (group iv) and FeGd-HN@TA-Fe^{2+}-3-SN38-2 (group v) show obvious tumor growth inhibition with the first mouse euthanized at day 36 and 56, respectively. FeGd-HN@TA-Fe^{2+}-3-SN38-2 + αPD-L1 (group vi) exhibits more remarkable inhibition of tumor growth with all mice survived. The significant statistical difference ($p < 0.001$) between FeGd-HN@TA-Fe^{2+}-3-SN38-2 (group v) and PBS (group i) demonstrates the high efficacy of tumor immunoferroptosis synergistic therapy. The differences between FeGd-HN@TA-Fe^{2+}-3 (group iv) and FeGd-HN@TA-Fe^{2+}-3-SN38-2 (group v), and between FeGd-HN@TA-Fe^{2+}-3-

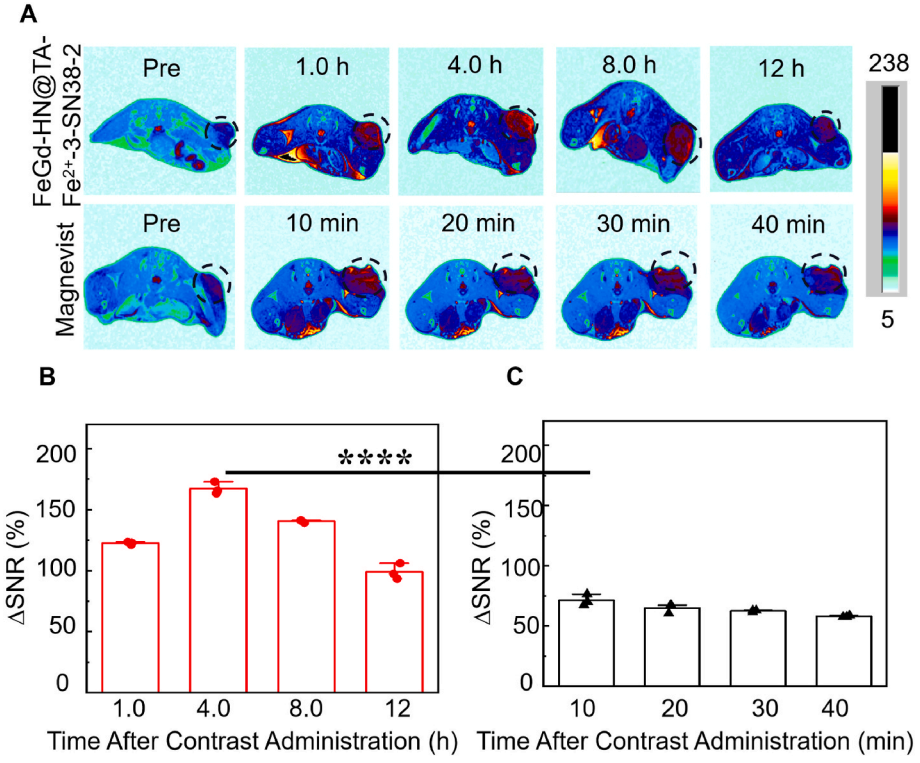

Fig. 4. (A): *In vivo* T_1-weighted MR images (slice orientation: axial; TR = 200.0 ms; TE = 6.3 ms) of 4T1 tumor-bearing BALB/c mice after *i.v.* injection of FeGd-HN@TA-Fe^{2+}-3-SN38-2 (Fe dosage: 5.0 mg/kg) or Magnevist (Gd dosage: 5.0 mg/kg). (B, C): The quantitative analysis of the MRI signal of tumors utilizing ΔSNR after *i.v.* injection of FeGd-HN@TA-Fe^{2+}-3-SN38-2 (B) or Magnevist (C). Mean ± SD, ****$P < 0.0001$.

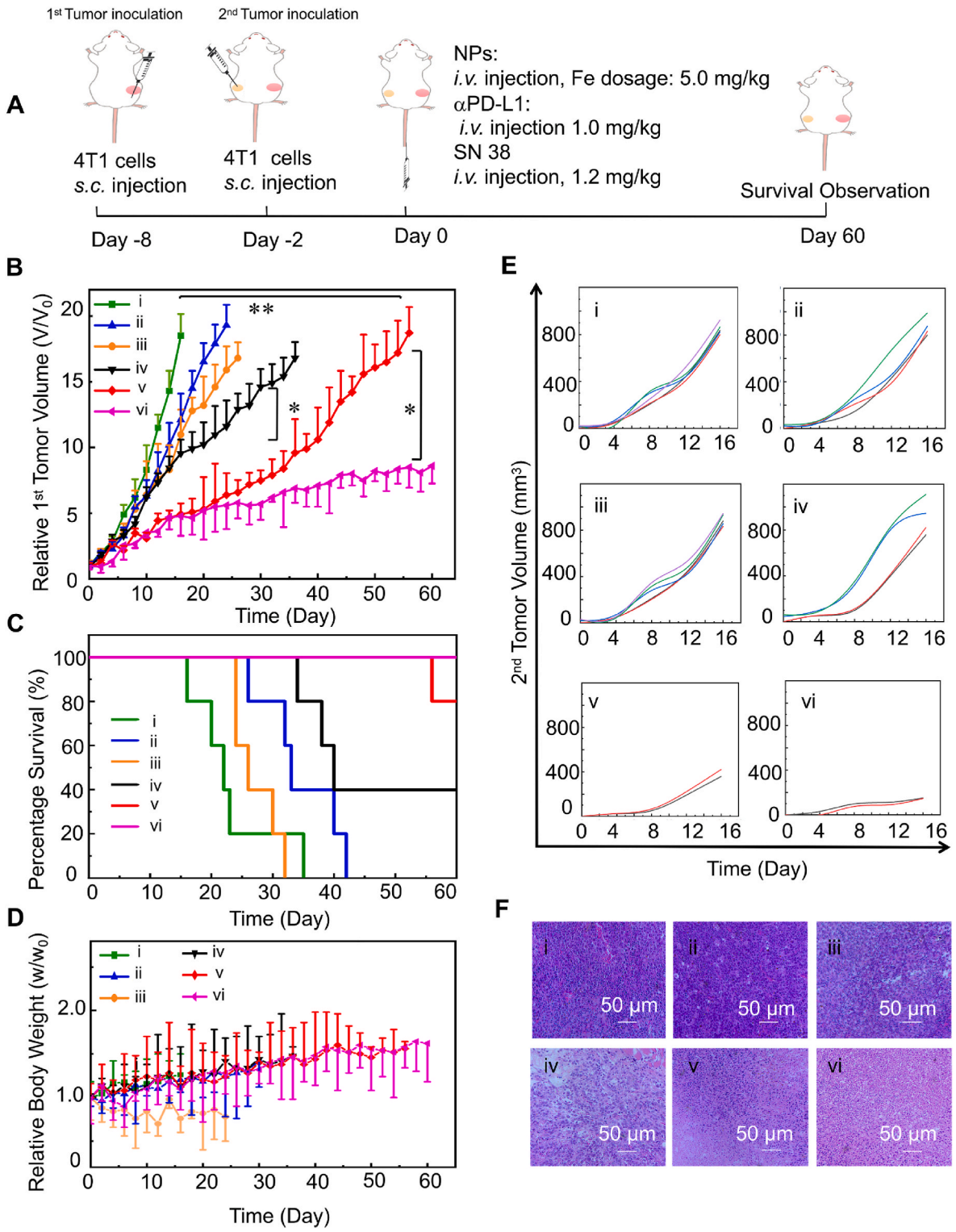

Fig. 5. (A): Schematic illustration of the animal experimental design. (B–E): 1st tumor growth curves (B), percentage survival (C), body weight changes (D), and 2nd tumor growth curves of the 4T1 tumor-bearing BALB/c mice (E), treated with (i) PBS (control), (ii) αPD-L1 (1.0 mg/kg), (iii) SN38 (1.2 mg/kg), (iv) FeGd-HN@TA-Fe^{2+}-3 (Fe dosage: 5.0 mg/kg), (v) FeGd-HN@TA-Fe^{2+}-3-SN38-2 (Fe dosage: 5.0 mg/kg), or (vi) FeGd-HN@TA-Fe^{2+}-3-SN38-2 + αPD-L1 (Fe dosage: 5.0 mg/kg, αPD-L1: 1.0 mg/kg). (F): H&E stainning of the tumor tissues from the 4T1 tumor-bearing mice with various treatments (i-vi) for 16 days. Mean ± SD, *P < 0.05, **P < 0.01.

SN38-2 (group v) and FeGd-HN@TA-Fe^{2+}-3-SN38-2 + αPD-L1 (group vi) are both statistically significant with $p < 0.01$, indicating the amplified efficacy of tumor ferroptosis therapy by immune modulation. Fig. 5D shows the relative body weight of mice during the process of tumor treatments. All groups show stable body weights, indicating low or non-toxicity of the treatments.

From the 2nd tumor growth curves (Fig. 5E), it can be seen that FeGd-HN@TA-Fe^{2+}-3-SN38-2 (group v) shows obvious tumor growth inhibition, indicating the function of immunoferroptosis synergistic therapy from FeGd-HN@TA-Fe^{2+}-3-SN38-2. In addition, FeGd-HN@TA-

Fe^{2+}-3-SN38-2 + αPD-L1 (group vi) shows more remarkable tumor growth inhibition, which demonstrates that the upregulation of $CD8^+$ T cells by immune checkpoints blockade (ICB) [13,74–78] can further amplify the efficacy of tumor therapy. The H&E stainning of the tumors from the 4T1 tumor-bearing mice with various treatments (i-vi) (Fig. 5F) reinforces the above-mentioned therapeutic efficacy.

The H&E assay of the main organs (heart, liver, spleen, lung, and kidney) as shown in Fig. S35 demonstrates the harmlessness of all groups, which reinforces the low or non-toxicity of the treatments. The hemolysis of FeGd-HN@TA-Fe^{2+}-3-SN38-2 with various Fe concentrations (Figs. S36A and B) is comparable to that of 0.90% of NaCl and PBS, but much lower than that of 1.0% of X-triton ($p < 0.0001$), which also demonstrate the bio-safety of FeGd-HN@TA-Fe^{2+}-3-SN38-2. Figs. S37 and S38 show the blood routine test and biochemical analysis of serum (liver function test) from the plasma Balb/c mice pre- or post-injection of FeGd-HN@TA-Fe^{2+}-3-SN38-2 (Fe dosage: 5.0 mg/kg or 15.0 mg/kg), demonstrating the bio-safety of FeGd-HN@TA-Fe^{2+}-3-SN38-2.

The CLSM images (Fig. S39) of the immunofluorescence of the kidney from the PBS or FeGd-HN@TA-Fe^{2+}-3-SN38-2 treated 4T1 tumor-bearing mice with stainning of anti-CD8, anti-CD4 and anti-CD3, suggest that FeGd-HN@TA-Fe^{2+}-3-SN38-2 treatment do not cause cytotoxic T-lymphocytes (CTLs) increase in kidney.

The optical images (Fig. S40) of the immunohistochemistry staining of hematoxylin and myeloperoxidase (MPO), demonstrate that FeGd-HN@TA-Fe^{2+}-3-SN38-2 treatment do not cause the increasing of neutrophil in kidney. All these data illustrate the bio-safety of FeGd-HN@TA-Fe^{2+}-3-SN38-2.

3.6. *The mechanisms of in vivo immunoferroptosis synergistic therapy by FeGd-HN@TA-Fe^{2+}-SN38*

Fig. 6A schematically illustrates the ferroptosis initiation, and the ferroptosis acceleration promoted by the STING activation *via* the GPX4 pathway. Typically, under the slight acidic TME, Fe^{2+} released from the FeGd-HN@TA-Fe^{2+}-3-SN38-2 generates ROS, leading to robust LPO accumulation and ferroptosis initiation. Meanwhile, the released SN38 activates the STING pathway, promoting the maturation of DCs. Furthermore, the cross-priming of matured DCs and T cells generates robust cytotoxic T-lymphocytes (CTLs), whose majority is $CD8^+$ T cells. The IFN-γ secreted from $CD8^+$ T cells inhibits system X_c^-, which downregulates the intracellular GSH/GPX4 and then promotes the ferroptosis acceleration. The corresponding mechanism was verified by the measurements of *in vivo* ROS, LPO, GPX4 and SLC7A11 levels. Fig. 6B shows the schematic illustration of the animal experimental design for determination of the ferroptosis indicators in the 4T1 tumor-bearing mice after treatment (*i.v.* injection) of (i) PBS (control), (ii) αPD-L1, (iii) SN38, (iv) FeGd-HN@TA-Fe^{2+}-3, (v) FeGd-HN@TA-Fe^{2+}-3-SN38-2, or (vi) FeGd-HN@TA-Fe^{2+}-3-SN38-2 + αPD-L1. Fig. 6C show the CLSM images with intratumor LPO accumulation stained by BOIDPY C11-581/591. It is found that FeGd-HN@TA-Fe^{2+}-3 (group iv) exhibits obvious fluorescence transition from red to green compared with the PBS (group i), αPD-L1 (group ii) and SN38 (group iii), indicating happening of ferroptosis. The green fluorescence of FeGd-HN@TA-Fe^{2+}-3-SN38-2 (group v) is much stronger than that of FeGd-HN@TA-Fe^{2+}-3 (group iv), demonstrating the STING activation by the released SN38 and the subsequent ferroptosis acceleration promoted by the STING activation *via* the GPX4 pathway. It presents the high efficiency of FeGd-HN@TA-Fe^{2+}-3-SN38-2 provoking FT at the tumor tissue, which is the most direct proof for immunotherapy synergy with ferroptosis. In addition, the green fluorescence of FeGd-HN@TA- Fe^{2+}-3-SN38-2 + αPD-L1 (group vi) is even stronger than that of FeGd-HN@TA- Fe^{2+}-3-SN38-2 (group v), which indicates the upregulation of $CD8^+$ T cells by ICB with enhancement of the IFN-γ secretion for subsequent ferroptosis acceleration *via* the GPX4 pathway. These conclusions can also be drawn from the fluorescence distriutions and relative quantification results of the cells in the treated tumors (i-vi) stained with DCFH-DA (Fig. 6D and E) for ROS analysis or with BOIDPY C11-581/591 (Fig. 6F and G) for LPO identification, measured by FC.

Furthermore, FeGd-HN@TA-Fe^{2+}-3-SN38-2 (group v) and FeGd-HN@TA-Fe^{2+}-3-SN38-2 + αPD-L1 (group vi) present much lower level of GPX4 (Fig. 6H) and SLC7A11 (Fig. 6I) in the treated tumors than that of the group i-iv. These results reinforce that the GPX4 pathway is the key target for the ferroptosis acceleration promoted by the SN38-based STING activation, or ICB-based $CD8^+$ T cells upregulation and its IFN-γ secretion.

Fig. 7A schematically presents the STING activation promoted by the GPX4 pathway based ferroptosis due to the enhanced exosomes release from the cells membrane ruptured by LPO. Typically, under the slight acidic TME and endosome conditions, Fe^{2+} and SN38 can be released from FeGd-HN@TA-Fe^{2+}-SN38. The released SN38 results in damaged cancer cells DNA and exocytosis of tumor-derived DNA fragments-containing exosomes. The released Fe^{2+} can initiate ferroptosis, and the corresponding LPO accumulation can lead to cell membranes rupture, which accelerates the exosomes exocytosis and promotes the STING activation. The activation of cGAS-STING pathway includes expression of STING protein, and secretion of IRF3 and IFN-β. The IFN-β plays the essential role of eliciting DCs maturation and cross-priming, leading to IFN-γ secretion from the $CD8^+$ T cells. The corresponding mechanism was verified by the measurements of *in vivo* immune indicators, including STING protein, IRF3, IFN-β and IFN-γ.

Fig. 7B shows the animal experimental design for determination of the above-mentioned immune indicators in the 4T1 tumor-bearing mice after treatment (*i.v.* injection) of PBS (group i), αPD-L1 (group ii), SN38 (group iii), FeGd-HN@TA-SN38-2 (group iv), FeGd-HN@TA-Fe^{2+}-3-SN38-2 (group v), or FeGd-HN@TA-Fe^{2+}-3-SN38-2 + αPD-L1 (group vi). The high expression of the STING, p-STING, IRF3, *p*-IRF3, TBK1 and *p*-TBK1 in the groups of FeGd-HN@TA-Fe^{2+}-3-SN38-2 (group v) and FeGd-HN@TA-Fe^{2+}-3-SN38-2 + αPD-L1 (group vi), as shown in Fig. 7C, demonstrates the successful activation of the STING pathways of intratumor DCs. The increasing secretion of IFN-β (Fig. 7D) and IFN-γ (Fig. 7E) in the tumor tissues of 4T1 tumor-bearing mice after the treatment with FeGd-HN@TA-Fe^{2+}-3-SN38-2 (group v) and FeGd-HN@TA-Fe^{2+}-3-SN38-2 + αPD-L1 (group vi) illustrates the maturation of DCs. Because the combination of αPD-L1 can upregulate the function of T cells, the FeGd-HN@TA-Fe^{2+}-3-SN38-2 + αPD-L1 (vi) group exhibts a higher intratumor level of IFN-γ than FeGd-HN@TA-Fe^{2+}-3-SN38-2 (v) group.

Moreover, the intratumor DCs analyzed by anti-CD11c, anti-CD80 and anti-CD86 (Fig. 7F and Fig. S41) suggests the maturation of DCs due to high expresion of CD80 and CD86 in the groups FeGd-HN@TA-Fe^{2+}-3-SN38-2 (v) and FeGd-HN@TA-Fe^{2+}-3-SN38-2 + αPD-L1 (group vi). The increased polulation of intratumor $CD8^+$ T cells and $CD4^+$ T cells analyzed by CD3, CD4 and CD8 (Fig. 7G and Fig. S42) demonstrate that the provoking of STING pathway by FeGd-HN@TA-Fe^{2+}-3-SN38-2 (v) can largely enhance the T cells profiling with robust CLTs inflitration of tumor tissue, and the combination of αPD-L1 with FeGd-HN@TA-Fe^{2+}-3-SN38-2 (group vi) can futher improve the effectiveness of T cells. Moreover, the $CD8^+$ T effective memeroy cells analyzed by CD8, CD62L and CD44 (Fig. 7H and Fig. S43) indicate the polulation of $CD8^+$ T effective memeory cells under STING activation after treatments of FeGd-HN@TA-Fe^{2+}-3-SN38-2 (group v) and FeGd-HN@TA-Fe^{2+}-3-SN38-2 + αPD-L1 (group vi). Moreover, the FeGd-HN@TA-Fe^{2+}-3 treatment also exihibits slight maturation of DCs and CTL polulation, which could be attributed to the ICD caused by intratumor ROS due to the ferroptosis, as shwon in Fig. S44.

It is well known that the triple negative breast cancer is the “cold” tumor with seldom immune cells infiltration. However, the 4T1-bearing mice treated by FeGd-HN@TA-Fe^{2+}-3-SN38-2 exhibits avtivation of immune cells (*e.g.*, DCs, $CD8^+$ T cells) with secretion of cytokines (*e.g.*, IFN-β and IFN-γ), which realizes the conversion of “cold tomor” to “hot tumor” [79,80]. These results demonstrate that the GPX4 pathway based ferroptosis promote the STING activation due to the enhanced exosomes

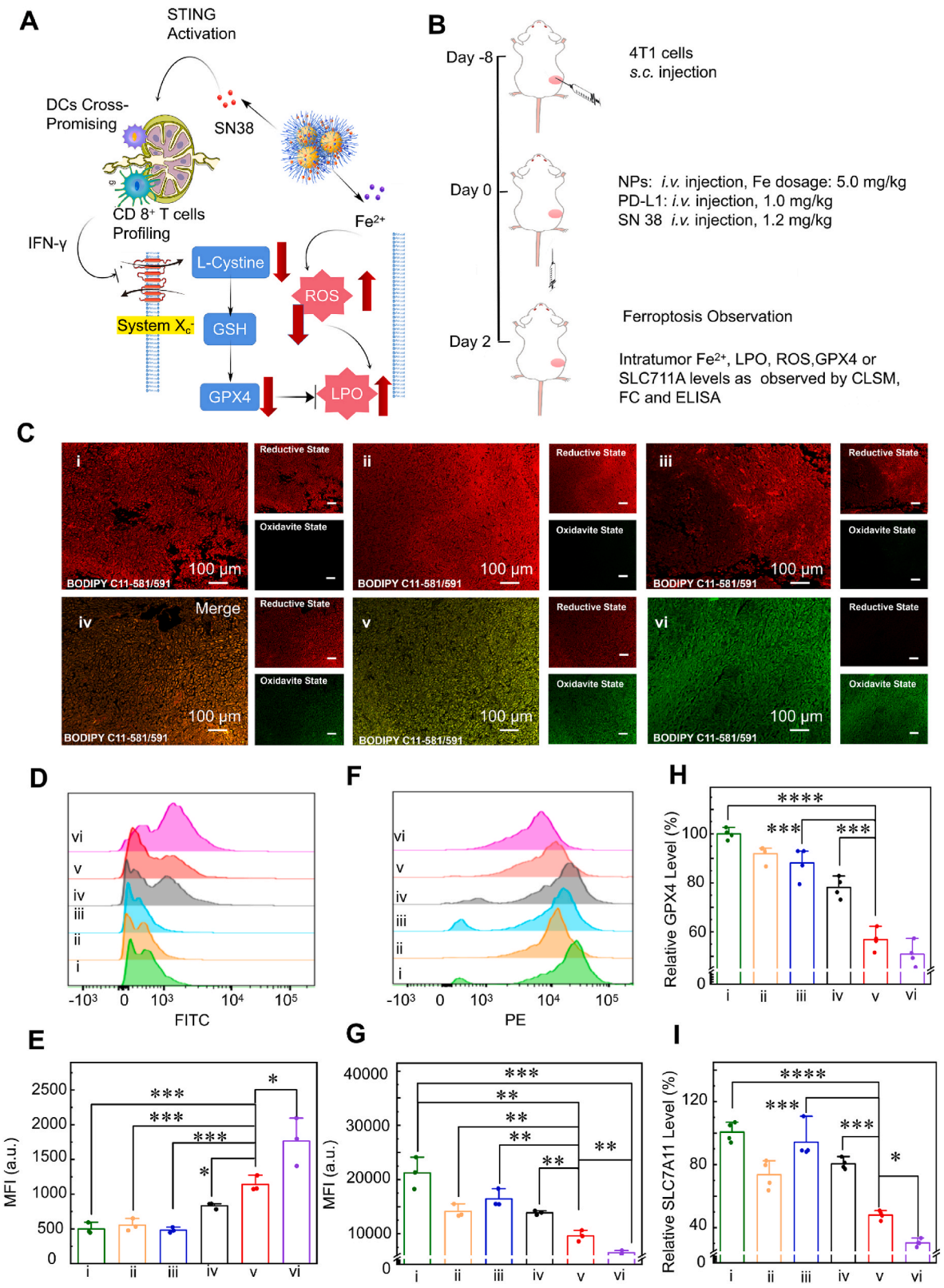

Fig. 6. (A): Schematic illustration of the ferroptosis initiation due to the ROS generation and LPO accumulation triggered by FeGd-HN@TA-Fe^{2+}-3-SN38-2, the STING activation by the released SN38, and the ferroptosis acceleration promoted by the STING activation *via* the GPX4 pathway. (B): Schematic illustration of the animal experimental design for determination of ferroptosis indicators in the 4T1 tumor-bearing mice after treatment (*i.v.* injection) of (i) PBS (control), (ii) αPD-L1 (1.0 mg/kg), (iii) SN38 (1.2 mg/kg), (iv) FeGd-HN@TA-Fe^{2+}-3 (Fe dosage: 5.0 mg/kg), (v) FeGd-HN@TA-Fe^{2+}-3-SN38-2 (Fe dosage: 5.0 mg/kg), or (vi) FeGd-HN@TA-Fe^{2+}-3-SN38-2 + αPD-L1 (Fe dosage: 5.0 mg/kg, αPD-L1: 1.0 mg/kg). (C): Observation of the LPO accumulation in the treated tumors (i-vi) stained with BOIDPY C11-581/591. (D–G): Fluorescence distriutions (D, F) and relative quanlitification (E, G) results of the cells in the treated tumors (i-vi) stained with DCFH-DA (D, E), and BOIDPY C11-581/591 (F, G). (H, I): The relative GPX4 (H) and SCL7A11 (I) levels of the cells in the treated tumors (i-vi). Mean ± SD, *P < 0.05, **P < 0.01, ***P < 0.001, ****P < 0.0001.

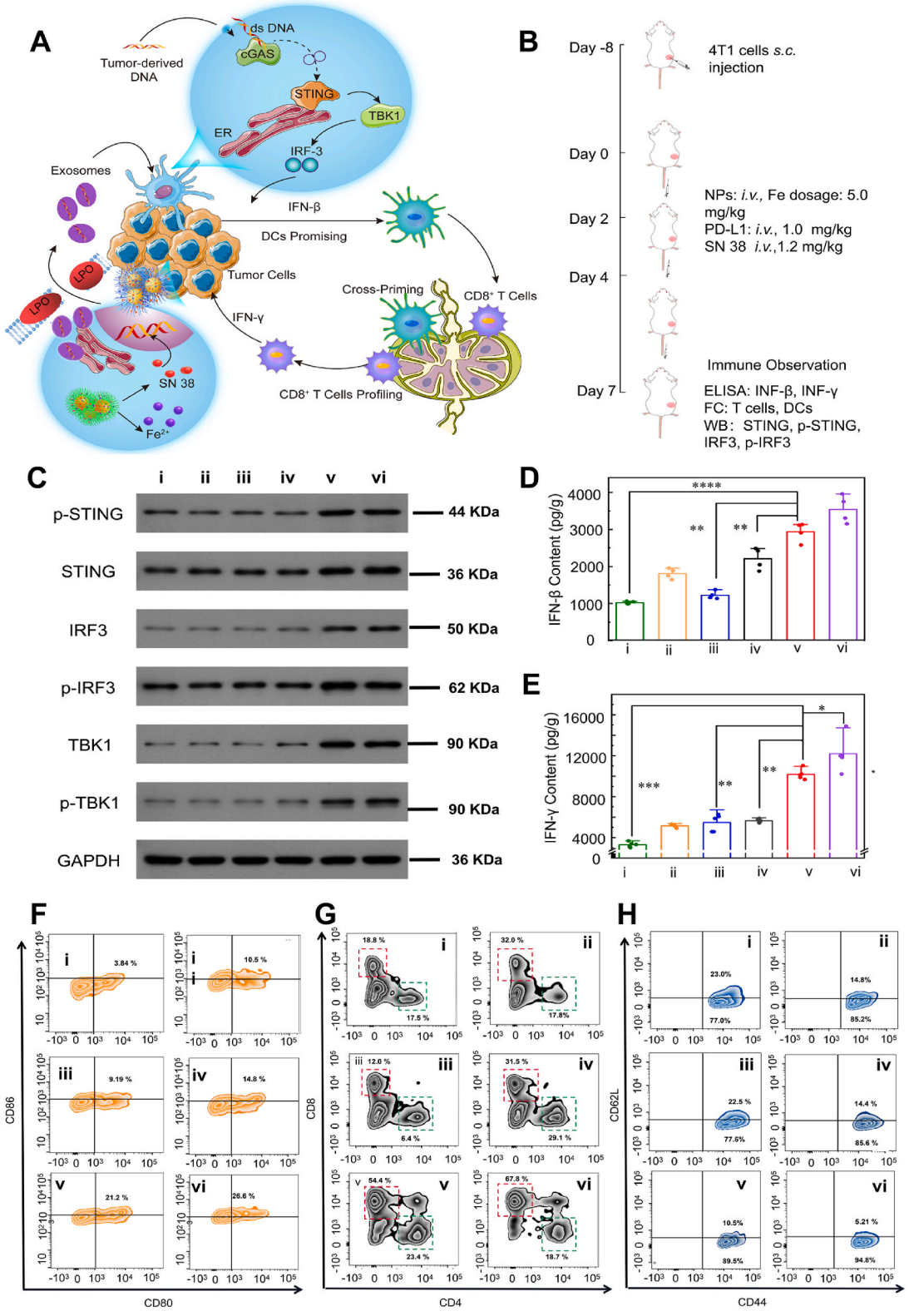

Fig. 7. (A): Schematic illustration for the STING activation promoted by the GPX4 pathway based ferroptosis due to the enhanced exosomes release from the cells membrane ruptured by LPO. (B): Schematic illustration of the animal experimental design for determination of immune indicators in the 4T1 tumor-bearing mice after treatment (*i.v.* injection) of (i) PBS (control), (ii) αPD-L1 (1.0 mg/kg), (iii) SN38 (1.2 mg/kg), (iv) FeGd-HN@TA-SN38-2 (SN38 dosage: 1.2 mg/kg), (v) FeGd-HN@TA-Fe^{2+}-3-SN38-2 (Fe dosage: 5.0 mg/kg; SN38 dosage: 1.2 mg/kg), or (vi) FeGd-HN@TA-Fe^{2+}-3-SN38-2 + αPD-L1 (Fe dosage: 5.0 mg/kg; αPD-L1: 2.5 μg/mice). (C) The intratumor expression of p-STING, STING, IRF3, *p*-IRF3, TBK1 and *p*-TBK1 of the 4T1 tumor-bearing mice as trated by i-vi. (D, E): The level of IFN-β (D) IRF3 and IFN-γ (E) secretion in the tumor tissues of 4T1 tumor-bearing mice after differenct treatments of (i-vi) analyzed by ELISA kits. (F–H): Flow cytometry examination of the intratumor DCs mautration (as analyzed by anti-CD11c, anti-CD80 and anti-CD86) (F), $CD8^+$ and $CD4^+$ T cells profilation (as analyzed by anti-CD3, anti-CD8 and anti-CD4) (G), and $CD8^+$ T effective memory cells profilation (as analyzed by anti-CD8, anti-CD62L and anti-CD44) (H) of the 4T1 tumor-bearing mice as treated by i-vi. Mean ± SD, *P < 0.05, **P < 0.01, ***P < 0.001, ****P < 0.0001.

release from the cells membrane ruptured by LPO.

4. Conclusions

In summary, a STING pathway-activatable MRI contrast agent (*i.e.*, FeGd-HN@TA-Fe^{2+}-SN38) was developed based on FeGd-HN nanoparticles. The successful coating of the TA, Fe^{2+} and SN38 are characterized by TEM, DLS, ICP, ESR, XPS, *etc.* The remarkable MRI performance of the FeGd-HN@TA-Fe^{2+}-SN38 is characterized by 3.0 and 7.0 T MRI scanners. CLSM images and FC analysis indicate the cellular uptake and endo/lysosome escape of FeGd-HN@TA-Fe^{2+}-SN38. The FeGd-HN@TA-Fe^{2+}-SN38 mediated ferroptosis therapy and its mechanism are confirmed on cells by observation and quantification of ROS, LPO, GSH and GPX4 with or without ferroptosis inhibitors, including Fer-1, DFO, GSH, L-cystine, NAC, and V_E. The FeGd-HN@TA-Fe2+-SN38 mediated immunotherapy and its mechanism are demonstrated by measuring the contents of exosomes and DNA, the expression of STING, IRF3, CD80 and CD86, and the exocytosis of cell cytokines IFN-β and IL-6. The half-life time ($t_{1/2}$) of FeGd-HN@TA-Fe^{2+}-SN38 in the blood stream is measured to be 2.41 h. The remarkable *in vivo* MRI performance of FeGd-HN@TA-Fe^{2+}-SN38 is attributed to its high accumulation at tumor location, the high relaxivities of FeGd-HN core, and the pH-sensitive TA-Fe^{2+}-SN38 layer that could be degraded in TME. The *in vivo* effectiveness and biosafety of the immunoferroptosis synergistic therapy induced by FeGd-HN@TA-Fe^{2+}-SN38 are demonstrated by the *in vivo* investigations on the 4T1 tumor-bearing mice. The mechanisms of *in vivo* immunoferroptosis synergistic therapy by FeGd-HN@TA-Fe^{2+}-SN38 are proved by measurements of *in vivo* ROS, LPO, GPX4 and SLC7A11 levels, the intratumor matured DCs analyzed by anti-CD11c-PE and anti-CD 11b-APC, the intratumor $CD8^+$ T cells analyzed by anti-CD4-FITC and anti-CD8-PE, the protein expresion of STING and IRF3, and the secretion of IFN-β and IFN-γ. Overall, our synthesized FeGd-HN@TA-Fe^{2+}-SN38 is a STING pathway-activatable contrast agent that can be used for MRI-guided tumor immunoferroptosis synergistic therapy with high efficacy.

Credit author statement

S. Guo, W. Xiong, Y. Xu and Z. Shen conceived the idea and designed the contrast agents for MRI-guided tumor immunoferroptosis synergistic therapy. S. Guo conducted most of the experiments, and prepared the original manuscript. W. Xiong, J. Zhu, R. Zhou, Q. Fan and Z. Li assisted with some of the experiments of ferroptosis characterization. Q. Zhang, P. Yi, Y. Feng assisted with the 7.0 T MRI measurements. W. Xiong, J. Feng, and Y. Xu provided help on the 3.0 T MRI measurements. J. Yang and H. Zhou assisted with some of the animal experiments. S. Yang, X. Qiu, Y. Xu and Z. Shen revised the manuscript.

Declaration of competing interest

The authors declare that they have no known competing financial interests or personal relationships that could have appeared to influence the work reported in this paper.

Data availability

Data will be made available on request.

Acknowledgements

This work was financially supported by Guangdong Provincial Natural Science Foundation of China (2021A1515010605), Guangzhou Key Research and Development Program of China (202103000094), and National Natural Science Foundation of China (32271374). All animal procedures were performed in accordance with the guidelines for Care and Use of Laboratory Animals of Southern Medical University, and approved by the Animal Ethics Committee of Southern Medical University. The assigned approval/accreditation number is SYXK(YUE) 2021-0167.

Appendix A. Supplementary data

Supplementary data to this article can be found online at https://doi.org/10.1016/j.biomaterials.2023.122300.

References

[1] X. Chen, C. Yu, R. Kang, G. Kroemer, D. Tang, Cellular degradation systems in ferroptosis, Cell Death Differ. 28 (2021) 1135–1148.
[2] W.S. Yang, R. SriRamaratnam, M.E. Welsch, K. Shimada, R. Skouta, V. S. Viswanathan, J.H. Cheah, P.A. Clemons, A.F. Shamji, C.B. Clish, L.M. Brown, A. W. Girotti, V.W. Cornish, S.L. Schreiber, B.R. Stockwell, Regulation of ferroptotic cancer cell death by GPX4, Cell 156 (2014) 317–331.
[3] L. Jiang, N. Kon, T. Li, S.-J. Wang, T. Su, H. Hibshoosh, R. Baer, W. Gu, Ferroptosis as a p53-mediated activity during tumour suppression, Nature 520 (2015) 57–62.
[4] S.J. Dixon, K.M. Lemberg, M.R. Lamprecht, R. Skouta, E.M. Zaitsev, C.E. Gleason, D.N. Patel, A.J. Bauer, A.M. Cantley, W.S. Yang, B. Morrison III, B.R. Stockwell, Ferroptosis: an iron-dependent form of nonapoptotic cell death, Cell 149 (2012) 1060–1072.
[5] W.S. Yang, B.R. Stockwell, Ferroptosis: death by lipid peroxidation, Trends Cell Biol. 26 (2016) 165–176.
[6] Y. Zou, M.J. Palte, A.A. Deik, H. Li, J.K. Eaton, W. Wang, Y.Y. Tseng, R. Deasy, M. Kost-Alimova, V. Dančík, E.S. Leshchiner, V.S. Viswanathan, S. Signoretti, T. K. Choueiri, J.S. Boehm, B.K. Wagner, J.G. Doench, C.B. Clish, P.A. Clemons, S. L. Schreiber, A GPX4-dependent cancer cell state underlies the clear-cell morphology and confers sensitivity to ferroptosis, Nat. Commun. 10 (2019) 1617.
[7] K. Bersuker, J.M. Hendricks, Z. Li, L. Magtanong, B. Ford, P.H. Tang, M.A. Roberts, B. Tong, T.J. Maimone, R. Zoncu, M.C. Bassik, D.K. Nomura, S.J. Dixon, J. A. Olzmann, The CoQ oxidoreductase FSP1 acts parallel to GPX4 to inhibit ferroptosis, Nature 575 (2019) 688–692.
[8] C. Mao, X. Liu, Y. Zhang, G. Lei, Y. Yan, H. Lee, P. Koppula, S. Wu, L. Zhuang, B. Fang, M.V. Poyurovsky, K. Olszewski, B. Gan, DHODH-mediated ferroptosis defence is a targetable vulnerability in cancer, Nature 593 (2021) 586–590.
[9] L. Zhou, C. Dong, L. Ding, W. Feng, L. Yu, X. Cui, Y. Chen, Targeting ferroptosis synergistically sensitizes apoptotic sonodynamic anti-tumor nanotherapy, Nano Today 39 (2021), 101212.
[10] W. Wang, J. Cai, J. Wen, X. Li, Y. Yu, L. Zhang, Q. Han, Z. Wei, Y. Ma, F. Ying, X. Xu, W. Li, Q. Yang, S. Sun, X. He, L. Cai, H. Xiao, Z. Wang, Boosting ferroptosis via abplatin(iv) for treatment of platinum-resistant recurrent ovarian cancer, Nano Today 44 (2022), 101459.
[11] Z.H. Li, Y. Chen, X. Zeng, X.Z. Zhang, Ultra-small FePt/siRNA loaded mesoporous silica nanoplatform to deplete cysteine for enhanced ferroptosis in breast tumor therapy, Nano Today 38 (2021), 101150.
[12] Y. Hao, L. Zhang, Z. Dong, C. Wang, Y. Chao, D. Zhao, Y. Zhu, Z. Yang, N. Yang, Y. Han, L. Feng, Z. Liu, Percutaneous implantation of ethanol fueled catalytic hydrogel suppresses tumor growth by triggering ferroptosis, Mater. Today 55 (2022) 7–20.
[13] K. Ni, T. Aung, S. Li, N. Fatuzzo, X. Liang, W. Lin, Nanoscale metal-organic Framework mediates radical therapy to enhance cancer immunotherapy, Chem 5 (2019) 1892–1913.
[14] S. Yue, P. Zhang, M. Qin, L. Zhu, Y. Qiao, Q. Li, Y. Lu, H. Wu, N. Jiang, C. Liu, M. A. Winnik, Y. Hou, An enzyme-like activity nanoprobe based on Fe(III)–rutin hydrate biomineral for MR imaging and therapy of triple negative breast cancer, Adv. Funct. Mater. 32 (2022), 2202848.
[15] Y. Du, R. Zhang, J. Yang, S. Liu, J. Zhou, R. Zhao, F. He, Y. Zhang, P. Yang, J. Lin, A "closed-loop" therapeutic strategy based on mutually reinforced ferroptosis and immunotherapy, Adv. Funct. Mater. 32 (2022), 2111784.
[16] T. Ding, Z. Wang, D. Xia, J. Zhu, J. Huang, Y. Xing, S. Wang, Y. Chen, J. Zhang, K. Cai, Long-lasting reactive oxygen species generation by porous redox mediator-potentiated nanoreactor for effective tumor therapy, Adv. Funct. Mater. 31 (2021), 2008573.
[17] T. Liu, W. Liu, M. Zhang, W. Yu, F. Gao, C. Li, S.-B. Wang, J. Feng, X.-Z. Zhang, Ferrous-supply-regeneration nanoengineering for cancer-cell-specific ferroptosis in combination with imaging-guided photodynamic therapy, ACS Nano 12 (2018) 12181–12192.
[18] C. Wu, Z. Liu, Z. Chen, D. Xu, L. Chen, H. Lin, J. Shi, A nonferrous ferroptosis-like strategy for antioxidant inhibitionsynergized nanocatalytic tumor therapeutics, Sci. Adv. 7 (2021), eabj8833.
[19] C.-C. Xue, M.-H. Li, Y. Zhao, J. Zhou, Y. Hu, K.-Y. Cai, Y. Zhao, S.-H. Yu, Z. Luo, Tumor microenvironment-activatable Fe-doxorubicin preloaded amorphous $CaCO_3$ nanoformulation triggers ferroptosis in target tumor cells, Sci. Adv. 6 (2020), eaax1346.
[20] C.M. Bebber, E.S. Thomas, J. Stroh, Z. Chen, A. Androulidaki, A. Schmitt, M. N. Höhne, L. Stüker, C. de Pádua Alves, A. Khonsari, M.A. Dammert, F. Parmaksiz, H.L. Tumbrink, F. Beleggia, M.L. Sos, J. Riemer, J. George, S. Brodesser, R. K. Thomas, H.C. Reinhardt, S. von Karstedt, Ferroptosis response segregates small cell lung cancer (SCLC) neuroendocrine subtypes, Nat. Commun. 12 (2021) 2048.

[21] J. Cai, Z. Ye, Y. Hu, L. Ye, L. Gao, Y. Wang, Q. sun, S. Tong, S. Zhang, L. Wu, J. a. Yang, Q. Chen, Fatostatin induces ferroptosis through inhibition of the AKT/mTORC1/GPX4 signaling pathway in glioblastoma, Cell Death Dis. 14 (2023) 211.

[22] W. Wang, M. Green, J.E. Choi, M. Gijón, P.D. Kennedy, J.K. Johnson, P. Liao, X. Lang, I. Kryczek, A. Sell, H. Xia, J. Zhou, G. Li, J. Li, W. Li, S. Wei, L. Vatan, H. Zhang, W. Szeliga, W. Gu, R. Liu, T.S. Lawrence, C. Lamb, Y. Tanno, M. Cieslik, E. Stone, G. Georgiou, T.A. Chan, A. Chinnaiyan, W. Zou, CD8$^+$ T cells regulate tumour ferroptosis during cancer immunotherapy, Nature 569 (2019) 270–274.

[23] S. Li, M. Luo, Z. Wang, Q. Feng, J. Wilhelm, X. Wang, W. Li, J. Wang, A. Cholka, Y.-x. Fu, B.D. Sumer, H. Yu, J. Gao, Prolonged activation of innate immune pathways by a polyvalent STING agonist, Nat. Biomed. Eng. 5 (2021) 455–466.

[24] M. Luo, H. Wang, Z. Wang, H. Cai, Z. Lu, Y. Li, M. Du, G. Huang, C. Wang, X. Chen, M.R. Porembka, J. Lea, A.E. Frankel, Y.X. Fu, Z.J. Chen, J. Gao, A STING-activating nanovaccine for cancer immunotherapy, Nat. Nanotech. 12 (2017) 648–654.

[25] C. Wang, R. Zhang, X. Wei, M. Lv, Z. Jiang, Metalloimmunology: the metal ion-controlled immunity, Adv. Immunol. 145 (2020) 187–241.

[26] T.F. Gajewski, E.F. Higgs, Immunotherapy with a sting, Science 369 (2020) 921–922.

[27] Q. Jin, W. Zhu, J. Zhu, J. Zhu, J. Shen, Z. Liu, Y. Yang, Q. Chen, Nanoparticle-mediated delivery of inhaled immunotherapeutics for treating lung metastasis, Adv. Mater. 33 (2021), e2007557.

[28] D. Shae, J.J. Baljon, M. Wehbe, P.P. Christov, K.W. Becker, A. Kumar, N. Suryadevara, C.S. Carson, C.R. Palmer, F.C. Knight, S. Joyce, J.T. Wilson, Co-delivery of peptide neoantigens and stimulator of interferon genes agonists enhances response to cancer vaccines, ACS Nano 14 (2020) 9904–9916.

[29] L. Hou, C. Tian, Y. Yan, L. Zhang, H. Zhang, Z. Zhang, Manganese-based nanoactivator optimizes cancer immunotherapy *via* enhancing innate immunity, ACS Nano 14 (2020) 3927–3940.

[30] C.G. Park, C.A. Hartl, D. Schmid, E.M. Carmona, H.-J. Kim, M.S. Goldberg, Extended release of perioperative immunotherapy prevents tumor recurrence and eliminates metastases, Sci. Transl. Med. 10 (2018), eaar1916.

[31] J. Chen, M. Qiu, Z. Ye, T. Nyalile, Y. Li, Z. Glass, X. Zhao, L. Yang, J. Chen, Q. Xu, In situ cancer vaccination using lipidoid nanoparticles, Sci. Adv. 7 (2021), eabf1244.

[32] W. Li, L. Lu, J. Lu, X. Wang, C. Yang, J. Jin, L. Wu, X. Hong, F. Li, D. Cao, Y. Yang, M. Wu, B. Su, J. Cheng, X. Yang, W. Di, L. Deng, cGAS-STING–mediated DNA sensing maintains CD8$^+$ T cell stemness and promotes antitumor T cell therapy, Sci. Transl. Med. 12 (549) (2020), eaay9013.

[33] E.N. Chin, C. Yu, V.F. Vartabedian, Y. Jia, M. Kumar, A.M. Gamo, W. Vernier, S. H. Ali, M. Kissai, D.C. Lazar, N. Nguyen, L.E. Pereira, B. Benish, A.K. Woods, S. B. Joseph, A. Chu, K.A. Johnson, P.N. Sander, F. Martínez-Peña, E.N. Hampton, T. S. Young, D.W. Wolan, A.K. Chatterjee, P.G. Schultz, H.M. Petrassi, J.R. Teijaro, L. L. Lairson, Antitumor activity of a systemic STING-activating non-nucleotide cGAMP mimetic, Sciencde 369 (2020) 993–999.

[34] B. Jneid, A. Bochnakian, C. Hoffmann, F. Delisle, E. Djacoto, P. Sirven, J. Denizeau, C. Sedlik, Y. Gerber-Ferder, F. Fiore, R. Akyol, C. Brousse, R. Kramer, I. Walters, S. Carlioz, H. Salmon, B. Malissen, M. Dalod, E. Piaggio, N. Manel, Selective STING stimulation in dendritic cells primes antitumor T cell responses, Sci. Immunol. 8 (79) (2023), eabn6612.

[35] X. Sun, X. Zhou, Y.L. Lei, J.J. Moon, Unlocking the promise of systemic STING agonist for cancer immunotherapy, J. Contr. Release 357 (2023) 417–421.

[36] S. Liu, B. Yang, Y. Hou, K. Cui, X. Yang, X. Li, L. Chen, S. Liu, Z. Zhang, Y. Jia, Y. Xie, Y. Xue, X. Li, B. Yan, C. Wu, W. Deng, J. Qi, D. Lu, G.F. Gao, P. Wang, G. Shang, The mechanism of STING autoinhibition and activation, Mol. Cell 83 (2023) 1502–1518.e10.

[37] P. Zhang, A. Rashidi, J. Zhao, C. Silvers, H. Wang, B. Castro, A. Ellingwood, Y. Han, A. Lopez-Rosas, M. Zannikou, C. Dmello, R. Levine, T. Xiao, A. Cordero, A. M. Sonabend, I.V. Balyasnikova, C. Lee-Chang, J. Miska, M.S. Lesniak, STING agonist-loaded, CD47/PD-L1-targeting nanoparticles potentiate antitumor immunity and radiotherapy for glioblastoma, Nat. Commun. 14 (2023) 1610.

[38] K. Yang, W. Han, X. Jiang, A. Piffko, J. Bugno, C. Han, S. Li, H. Liang, Z. Xu, W. Zheng, L. Wang, J. Wang, X. Huang, J.P.Y. Ting, Y.-X. Fu, W. Lin, R. R. Weichselbaum, Zinc cyclic di-AMP nanoparticles target and suppress tumours *via* endothelial STING activation and tumour-associated macrophage reinvigoration, Nat. Nanotech. 17 (2022) 1322–1331.

[39] F. Chen, T. Li, H. Zhang, M. Saeed, X. Liu, L. Huang, X. Wang, J. Gao, B. Hou, Y. Lai, C. Ding, Z. Xu, Z. Xie, M. Luo, H. Yu, Acid-ionizable iron nanoadjuvant augments STING activation for personalized vaccination immunotherapy of cancer, Adv. Mater. 35 (2023), 2209910.

[40] T. Li, R. Song, F. Sun, M. Saeed, X. Guo, J. Ye, F. Chen, B. Hou, Q. Zhu, Y. Wang, C. Xie, L. Tang, Z. Xu, H. Xu, H. Yu, Bioinspired magnetic nanocomplexes amplifying STING activation of tumor-associated macrophages to potentiate cancer immunotherapy, Nano Today 43 (2022), 101400.

[41] L. Zhou, B. Hou, D. Wang, F. Sun, R. Song, Q. Shao, H. Wang, H. Yu, Y. Li, Engineering polymeric prodrug nanoplatform for vaccination immunotherapy of cancer, Nano Lett. 20 (6) (2020) 4393–4402.

[42] J. Zhao, S. Ma, Y. Xu, X. Si, H. Yao, Z. Huang, Y. Zhang, H. Yu, Z. Tang, W. Song, X. Chen, In situ activation of STING pathway with polymeric SN38 for cancer chemoimmunotherapy, Biomaterials 268 (2021), 120542.

[43] S. Li, B. Mirlekar, B.M. Johnson, W.J. Brickey, J.A. Wrobel, N. Yang, D. Song, S. Entwistle, X. Tan, M. Deng, Y. Cui, W. Li, B.G. Vincent, M. Gale Jr., Y. Pylayeva-Gupta, J.P. Ting, STING-induced regulatory B cells compromise NK function in cancer immunity, Nature 610 (2022) 373–380.

[44] L. Cao, H. Tian, M. Fang, Z. Xu, D. Tang, J. Chen, J. Yin, H. Xiao, K. Shang, H. Han, X. Li, Activating cGAS-STING pathway with ROS-responsive nanoparticles delivering a hybrid prodrug for enhanced chemo-immunotherapy, Biomaterials 290 (2022), 121856.

[45] Q. Lu, R. Chen, S. Du, C. Chen, Y. Pan, X. Luan, J. Yang, F. Zeng, B. He, X. Han, Y. Song, Activation of the cGAS-STING pathway combined with CRISPR-Cas9 gene editing triggering long-term immunotherapy, Biomaterials 291 (2022), 121871.

[46] Z. Sun, Z. Wang, T. Wang, J. Wang, H. Zhang, Z. Li, S. Wang, F. Sheng, J. Yu, Y. Hou, Biodegradable MnO-based nanoparticles with engineering surface for tumor therapy: simultaneous fenton-like ion delivery and immune activation, ACS Nano 16 (8) (2022) 11862–11875.

[47] R. Yue, C. Zhang, L. Xu, Y. Wang, G. Guan, L. Lei, X. Zhang, G. Song , Dual key co-activated nanoplatform for switchable MRI monitoring accurate ferroptosis-based synergistic therapy, Chem 8(7) 1956-1981.

[48] Z. Shen, J. Song, Z. Zhou, B.C. Yung, M.A. Aronova, Y. Li, Y. Dai, W. Fan, Y. Liu, Z. Li, H. Ruan, R.D. Leapman, L. Lin, G. Niu, X. Chen, A. Wu, Dotted core–shell nanoparticles for T_1-weighted MRI of tumors, Adv. Mater. 30 (2018), 1803163.

[49] E. Blanco, H. Shen, M. Ferrari, Principles of nanoparticle design for overcoming biological barriers to drug delivery, Nat. Biotechnol. 33 (9) (2015) 941–951.

[50] L. Huang, J. Feng, W. Fan, W. Tang, X. Rong, W. Liao, Z. Wei, Y. Xu, A. Wu, X. Chen, Z. Shen, Intelligent pore switch of hollow mesoporous organosilica nanoparticles for high contrast magnetic resonance imaging and tumor-specific chemotherapy, Nano Lett. 21 (2021) 9551–9559.

[51] S. Guo, Z. Li, J. Feng, W. Xiong, J. Yang, X. Lu, S. Yang, Y. Xu, A. Wu, Z. Shen, Cycloacceleration of ferroptosis and calcicoptosis for magnetic resonance imaging-guided colorectal cancer therapy, Nano Today 47 (2022), 101663.

[52] A. Martínez-Chávez, H. Rosing, C. Gan, Y. Wang, A.H. Schinkel, J.H. Beijnen, Bioanalytical method for the simultaneous quantification of irinotecan and its active metabolite SN-38 in mouse plasma and tissue homogenates using HPLC-fluorescence, J. Chromatogr., B: Anal. Technol. Biomed. Life Sci. 1149 (2020), 122177.

[53] M.P. Kabir, Y. Orozco-Gonzalez, G. Hastings, S. Gozem, The effect of hydrogen-bonding on flavin's infrared absorption spectrum, Spectrochim. Acta, Part A 262 (2021), 120110.

[54] Q. Chen, X. Shan, S. Shi, C. Jiang, T. Li, S. Wei, X. Zhang, G. Sun, J. Liu, Tumor microenvironment-responsive polydopamine-based core/shell nanoplatform for synergetic theranostics, J. Mater. Chem. B 8 (2020) 4056–4066.

[55] Z. Shen, T. Chen, X. Ma, W. Ren, Z. Zhou, G. Zhu, A. Zhang, Y. Liu, J. Song, Z. Li, H. Ruan, W. Fan, L. Lin, J. Munasinghe, X. Chen, A. Wu, Multifunctional theranostic nanoparticles based on exceedingly small magnetic iron oxide nanoparticles for T_1-weighted magnetic resonance imaging and chemotherapy, ACS Nano 11 (2017) 10992–11004.

[56] Z. Shen, J. Song, B.C. Yung, Z. Zhou, A. Wu, X. Chen, Emerging strategies of cancer therapy based on ferroptosis, Adv. Mater. 30 (2018), e1704007.

[57] M. Swietek, Y.H. Ma, N.P. Wu, A. Paruzel, W. Tokarz, D. Horak, Tannic acid coating augments glioblastoma cellular uptake of magnetic nanoparticles with antioxidant effects, Nanomaterials 12 (8) (2022).

[58] S. Yuan, C. Wei, G. Liu, L. Zhang, J. Li, L. Li, S. Cai, L. Fang, Sorafenib attenuates liver fibrosis by triggering hepatic stellate cell ferroptosis via HIF-1α/SLC7A11 pathway, Cell Prolif. 55 (2022), e13158.

[59] F. Ursini, M. Maiorino, Lipid peroxidation and ferroptosis: the role of GSH and GPX4, Free Radical Biol. Med. 152 (2020) 175–185.

[60] C. Hao, X. Wu, M. Sun, H. Zhang, A. Yuan, L. Xu, C. Xu, H. Kuang, Chiral Core–Shell Upconversion nanoparticle@MOF nanoassemblies for quantification and bioimaging of reactive oxygen species *in vivo*, J. Am. Chem. Soc. 141 (2019) 19373–19378.

[61] F. Shang, M. Lu, E. Dudek, J. Reddan, A. Taylor, Vitamin C and vitamin E restore the resistance of GSH-depleted lens cells to H_2O_2, Free Radical Biol. Med. 34 (5) (2003) 521–530.

[62] B. Wu, D.A. Liu, L. Guan, P.K. Myint, L. Chin, H. Dang, Y. Xu, J. Ren, T. Li, Z. Yu, S. Jabban, G.B. Mills, J. Nukpezah, Y.H. Chen, E.E. Furth, P.A. Gimotty, R.G. Wells, V.M. Weaver, R. Radhakrishnan, X.W. Wang, W. Guo, Stiff matrix induces exosome secretion to promote tumour growth, Nat. Cell Biol. 25 (3) (2023) 415–424.

[63] Q. Ouyang, Q. Chen, S. Ke, L. Ding, X. Yang, P. Rong, W. Feng, Y. Cao, Q. Wang, M. Li, S. Su, W. Wei, M. Liu, J. Liu, X. Zhang, J.Z. Li, H.Y. Wang, S. Chen, Rab8a as a mitochondrial receptor for lipid droplets in skeletal muscle, Dev. Cell 58 (4) (2023) 289–305.e6.

[64] K.N. Wang, L.Y. Liu, D. Mao, S. Xu, C.P. Tan, Q. Cao, Z.W. Mao, B. Liu, A polarity-sensitive ratiometric fluorescence probe for monitoring changes in lipid droplets and nucleus during ferroptosis, Angew. Chem. 60 (2021) 15095–15100.

[65] R. Patel, A. Santoro, P. Hofer, D. Tan, M. Oberer, A.T. Nelson, S. Konduri, D. Siegel, R. Zechner, A. Saghatelian, B.B. Kahn, ATGL is a biosynthetic enzyme for fatty acid esters of hydroxy fatty acids, Nature 606 (7916) (2022) 968–975.

[66] H. Liang, X. Wu, G. Zhao, K. Feng, K. Ni, X. Sun, Renal clearable ultrasmall single-crystal Fe nanoparticles for highly selective and effective ferroptosis therapy and immunotherapy, J. Am. Chem. Soc. 143 (38) (2021) 15812–15823.

[67] Y. Liu, W. Zhen, Y. Wang, S. Song, H. Zhang, $Na_2S_2O_8$ nanoparticles trigger antitumor immunotherapy through reactive oxygen species storm and surge of tumor osmolarity, J. Am. Chem. Soc. 142 (2020) 21751–21757.

[68] Z. Wan, H. Huang, R.E. West Iii, M. Zhang, B. Zhang, X. Cai, Z. Zhang, Z. Luo, Y. Chen, Y. Zhang, W. Xie, D. Yang, T.D. Nolin, J. Wang, S. Li, J. Sun, Overcoming pancreatic cancer immune resistance by codelivery of CCR2 antagonist using a STING-activating gemcitabine-based nanocarrier, Mater. Today 62 (2023) 33–50.

[69] Z. Shen, W. Fan, Z. Yang, Y. Liu, V.I. Bregadze, S.K. Mandal, B.C. Yung, L. Lin, T. Liu, W. Tang, L. Shan, Y. Liu, S. Zhu, S. Wang, W. Yang, L.H. Bryant, D. T. Nguyen, A. Wu, X. Chen, Exceedingly small gadolinium oxide nanoparticles with remarkable relaxivities for magnetic resonance imaging of tumors, Small 15 (2019), 1903422.

[70] G. Wang, L. Xie, B. Li, W. Sang, J. Yan, J. Li, H. Tian, W. Li, Z. Zhang, Y. Tian, Y. Dai, A nanounit strategy reverses immune suppression of exosomal PD-L1 and is associated with enhanced ferroptosis, Nat. Commun. 12 (2021) 5733.
[71] J. Ye, B. Hou, M. Saeed, Z. Xu, H. Yu, Engineering bioinspired nanomedicines to mitigate the resistance to cancer immunotherapy, Acc. Mater. Res. 3 (2022) 697–708.
[72] J.H. Li, L.J. Huang, H.L. Zhou, Y.M. Shan, F.M. Chen, V.P. Lehto, W.J. Xu, L.Q. Luo, H.J. Yu, Engineered nanomedicines block the PD-1/PD-L1 axis for potentiated cancer immunotherapy, Acta Pharmacol. Sin. 43 (11) (2022) 2749–2758.
[73] J. Gao, H. Zhang, F. Zhou, B. Hou, M. Chen, Z. Xie, H. Yu, Acid-activatible micelleplex delivering siRNA-PD-L1 for improved cancer immunotherapy of CDK4/6 inhibition, Chin. Chem. Lett. 32 (6) (2021) 1929–1936.
[74] C. Sun, R. Mezzadra, T.N. Schumacher, Regulation and function of the PD-L1 checkpoint, Immunity 48 (3) (2018) 434–452.
[75] D.B. Johnson, C.A. Nebhan, J.J. Moslehi, J.M. Balko, Immune-checkpoint inhibitors: long-term implications of toxicity, Nat. Rev. Clin. Oncol. 19 (2022) 254–267.
[76] X. Guan, F. Polesso, C. Wang, A. Sehrawat, R.M. Hawkins, S.E. Murray, G. V. Thomas, B. Caruso, R.F. Thompson, M.A. Wood, C. Hipfinger, S.A. Hammond, J. N. Graff, Z. Xia, A.E. Moran, Androgen receptor activity in T cells limits checkpoint blockade efficacy, Nature 60 (2022) 791–796.
[77] H. Tang, X. Xu, Y. Chen, H. Xin, T. Wan, B. Li, H. Pan, D. Li, Y. Ping, Reprogramming the tumor microenvironment through second-near-infrared-window photothermal genome editing of PD-L1 mediated by supramolecular gold nanorods for enhanced cancer immunotherapy, Adv. Mater. 33 (2021), e2006003.
[78] J.H. Cha, L.C. Chan, C.W. Li, J.L. Hsu, M.C. Hung, Mechanisms controlling PD-L1 expression in cancer, Mol. Cell 76 (2019) 359–370.
[79] M. Wu, D. Zheng, D. Zhang, P. Yu, L. Peng, F. Chen, Z. Lin, Z. Cai, J. Li, Z. Wei, X. Lin, J. Liu, X. Liu, Converting immune cold into hot by biosynthetic functional vesicles to boost systematic antitumor immunity, iScience 23 (2020), 101341.
[80] R. Song, T. Li, J. Ye, F. Sun, B. Hou, M. Saeed, J. Gao, Y. Wang, Q. Zhu, Z. Xu, H. Yu, Acidity-activatable dynamic aanoparticles boosting ferroptotic cell death for immunotherapy of cancer, Adv. Mater. 33 (2021), 2101155.